Check for updates

An Efficient Inexact Gauss–Seidel-Based Algorithm for Image Restoration with Mixed Noise

Tingting Wu[1] · **Yue Min**[1] · **Chaoyan Huang**[2] · **Zhi Li**[3] · **Zhongming Wu**[4] · **Tieyong Zeng**[2]

Abstract

A challenge in image restoration is to recover a clear image from the blurry observation in the presence of different types of noise. There are few works addressing image deblurring under mixed noise. To handle this issue, we propose a general model based on classical wavelet tight frame regularization. We utilize a convexity-preserving term to obtain a component-wise convex model under a mild condition. Indeed, to reduce the cost of solving subproblems, the inexact Gauss–Seidel-based majorized semi-proximal alternating direction method of multipliers (sGS-imsPADMM) with relative error control is developed. Besides, the global convergence of sGS-imsPADMM is demonstrated. Numerical results for the image restoration problems show that the proposed model and solving approach are superior to some state-of-the-art methods both in numerical analysis and visual quality.

✉ Tieyong Zeng
  zeng@math.cuhk.edu.hk

  Tingting Wu
  wutt@njupt.edu.cn

  Yue Min
  1021082412@njupt.edu.cn

  Chaoyan Huang
  cyhuang@math.cuhk.edu.hk

  Zhi Li
  zli@cs.ecnu.edu.cn

  Zhongming Wu
  wuzm@nuist.edu.cn

1   School of Science, Nanjing University of Posts and Telecommunications, Nanjing 210023, China

2   Department of Mathematics, The Chinese University of Hong Kong, Shatin, Hong Kong, SAR, China

3   Shanghai Key Laboratory of Multidimensional Information Processing, Department of Computer Science and Technology, East China Normal University, Shanghai 200241, China

4   School of Management Science and Engineering, Nanjing University of Information Science and Technology, Nanjing 210044, China

1 Introduction

In the field of image processing, recovering clear images from blurred and noisy observations is a fundamental task. Image degradation occurs when acquisition equipment or lighting affects the image. Therefore, images obtained from devices or machines can be corrupted by various types of 'pollution', such as noise and blur. Hence, image denoising and deblurring have received significant attention in applied mathematics over the years. Noise is a useless signal, and two types of noise have been widely studied: additive noise [23, 26, 28] and multiplication noise [24, 25, 27].

Additive noise is a random process independent of the signal. If vector b is the additive Gaussian noise with standard variance σ and mean 0, the degraded image f is formulated as

$$f = Hw + b, \tag{1}$$

where w represents the original image, and H is a linear operator. Many methods have been developed to recover w from f, such as variational-based methods [12, 20], nonlocal methods [13, 26], wavelet-based methods [23, 28], and so on. Among these methods, the regularization methods based on total variation (TV) and the wavelet frame were widely used to handle the additive noise with deblurring simultaneously. For instance, the Rudin-Osher-Fatemi (ROF) model [31] based on TV has been widely used. Differing from the TV-based regularization, wavelet frame based approaches have also been widely used due to their multi-resolution structure, sparse representations, and high redundancy [23].

On the other hand, multiplicative noise is proportional to the signal, and the noise model with blur can be formulated as

$$f = Hw\eta, \tag{2}$$

where η denotes multiplicative noise, which follows standard distributions such as Gamma distributions. The probability density function of multiplicative Gamma noise [2] is defined as

$$p(\eta; K) = \frac{K^K}{(K)}\eta^{K-1}e^{-K\eta}\mathbf{1}_{\{\eta \geq 0\}}, \tag{3}$$

where $\mathbf{1}_{\{\eta \geq 0\}}$ represents the indicator function of the subset $\{\eta | \eta \geq 0\}$, $\Gamma(\cdot)$ is the classical Gamma function, η follows a gamma law with mean 1, and the variance of η is $1/K$. The integer K determines the level of the Gamma noise.

Methods employed in literature for multiplicative noise and blur removal include diffusion equation methods [32, 38], nonlocal low-rank based methods [15, 24], and variational-based methods [4, 40]. In these methods, Rudin, Lions and Osher [30] introduced TV regularization to multiplicative noise and proposed the first variational model, known as the RLO model. However, the RLO model cannot produce effective results in restoring Gamma noise. Aubert and Aujol [2] introduced a second variational model, referred to as the AA model, which employed Bayesian Maximum A Posteriori (MAP) probability estimation. The authors in [2] expanded the denoising model to handle the deblurring problem, in which the gradient projection-based algorithm was used in their model. Because of the nonconvexity of the AA model, the resulting optimization problem is not easy to solve. To overcome this difficulty,

Dong and Zeng [11] proposed two models for image restoration. The first model, denoted as the DZ model, is a generalized model that modifies the data fidelity term by adding a quadratic penalty term. This modification guarantees the convexity of the objective function under mild conditions. The second model is a strictly convex model that guarantees the uniqueness of the solution. Dong and Zeng achieved this by using the I-divergence technique. To solve the convex models, they used the split Bregman algorithm. Through the use of the logarithm to transform the multiplicative noise and blur removal problem into the additive noise and blur removal problem, Shi and Osher [33] proposed an SO model with a quadratic term, which is globally convex. The experimental results demonstrate that these TV regularization-based models have good performance in image restoration, such as effectively preserving edges and details in images, whereas stair-casing artifacts would be inevitable with TV.

The wavelet frames-based regularization method is a typical sparsity-based method for image restoration. There are three different types of wavelet models, i.e., analysis-based models [1, 5], synthesis-based models [6, 10], and balance models [3, 7]. In the analysis-based approach, assuming that the wavelet tight frame coefficient W of the natural image w is sparse, the size of Ww can adaptively represent the regularity of the underlying image. Due to the redundancy and multi-resolution structure of the wavelet tight frame, the wavelet-based approach can significantly improve the quality of the recovered image.

In reality, however, the type of noise may be neither additive nor multiplicative. Instead, it might be a mixture of the same type [16, 36] or a mixture of these two types [18, 35]. However, the previously mentioned methods can not deal with this problem directly. Recently, many methods have been proposed to solve mixed noise. Thanh et al. [34] proposed a model based on TV to deal with a mixture of Poisson-Gaussian noise. Wang et al. [36] proposed an adaptive algorithm based on CNN deep learning, namely EM-CNN. It combined traditional variational methods and deep learning-based algorithms to remove Gaussian-Gaussian noise or Gaussian-impulse noise. Some works also have been proposed for removing mixed Gaussian-Gamma noise. Ullah et al. [35] proposed a new model using a linear combination of the fractional total variation, image priors, and the data fidelity term in [31]. They used an empirical selection of the parameters to balance the above three items. Huang et al. [14] focused on variational approaches to obtain restorations. Since the model was non-convex, a convex relaxation model was proposed. Although those methods present competitive performance in handling mixture noise removal task, they perform mediocrely in deblurring tasks, such as the boundaries are still blurred.

In this paper, the restoration of blurred images corrupted by a mixture of additive Gaussian noise and multiplicative Gamma noise is studied. The mathematical expression of the degraded image f is formulated as follows:

$$f = (Hw + b)\eta. \tag{4}$$

To address this issue, we propose a novel model that uses regularizer based on wavelet tight frame. Specifically, our model incorporates a convexity-preserving term, which ensures that the objective function is convex under mild conditions. By using wavelet tight frame as a regularization term, our model is able to preserve image details while removing noise and blurring. Then, we develop an inexact symmetric Gauss–Seidel-based majorized semi-proximal alternating direction method of multipliers (sGS-imsPADMM) with relative error control for solving the proposed model. The experiments demonstrate that the proposed method is well suited to mixed noise and blur removal simultaneously. The main contributions of this work are three-fold:

- We propose a novel convex model to deal with degraded images corrupted by mixed Gaussian-Gamma noise and blur. We utilize the convexity preserving term and wavelet tight frame regularization into the non-convex model to obtain a solvable convex model.
- We develop an inexact sGS-imsPADMM with relative error control for solving the proposed model because it can reduce the cost of solving subproblems and achieve appropriate accuracy. Although sGS-imsPADMM has not been widely considered in imaging science, it is a nice example explaining the excellent performance of the algorithm that can be applied to image processing problems.
- The extensive experiments demonstrated that the proposed model surpasses state-of-the-art models in removing mixed Gaussian-Gamma noise as well as blur. Moreover, the proposed inexact sGS-imsPADMM approach with relative error control can achieve a better solution in terms of restoration quality while also being faster than other methods like ADMM.

The rest of the paper is organized as follows. In Sect. 2, the related models for restoring blurred images with mixed noise are briefly reviewed, and we propose a novel model for mixed noise and blur removal. Section 3 presents an iterative algorithm for solving corresponding convex optimization problems and gives the convergence analysis. In Sect. 4, some numerical experiments are conducted to demonstrate the efficiency and superiority of the proposed model and solving method. Section 5 concludes this paper.

2 A Novel Model for Denoising and Deblurring

In this section, we give a review of some related models in image restoration. Then, we propose a novel model by using a regularizer based on wavelet tight frame and a convexity-preserving term, to restore blurred images with Gaussian-Gamma noise.

As mentioned before, Huang et al. [14] introduced an intermediate image $u = Hw + b$ to derive a variational model from (4), in which u can be regarded as a convolution image with additive Gaussian noise b. In this approach, it is assumed that b is small. Moreover, it can be further assumed that $\inf f > 0$, then suppose that $0 < \sigma \leq 2\inf f$. The variational model [14] can be described as follows:

$$\min_{u>0,w} \left\langle \log u + \frac{f}{u}, 1 \right\rangle + \frac{\|Hw - u\|_2^2}{2\sigma^2} + \mu A(w), \tag{5}$$

where μ is a positive parameter. The last term $A(w)$ is a convex regularization term to prevent the model from over-fitting. Due to the non-convexity of the term $\log u$, the above model is non-convex and difficult to handle. To this end, they proposed to approximate the above model by a convex relaxation model.

Inspired by the convex relaxation model, we introduce a quadratic convex term to ensure that the model is component-wise convex on u. From this, a convex model for denoising and deblurring is proposed:

$$\min_{u>0,w} \left\langle \log u + \frac{f}{u}, 1 \right\rangle + \alpha \left\| \sqrt{u} - \sqrt{f} \right\|_2^2 + \frac{\|Hw - u\|_2^2}{2\sigma^2} + \mu A(w), \tag{6}$$

where α is a positive parameter. The preservation of convexity in the model not only guarantees its convexity but also enhances the overall effectiveness of image restoration to a certain degree. Further details on this matter will be discussed in the experimental section.

An important property of the image recovery process is the sparse representation of the image. The use of wavelet tight frame to represent an image is beneficial in ensuring the existence of sparsity. To demonstrate the advantages of the model's flexibility, we consider a model with wavelet tight frame regularization that can improve the performance of both deblurring and denoising of mixed noise, especially for Gaussian-Gamma noise. Generally, we propose the following model:

$$\min_{u>0,w} \left\langle \log u + \frac{f}{u}, 1 \right\rangle + \alpha \left\| \sqrt{u} - \sqrt{f} \right\|_2^2 + \frac{\|Hw - u\|_2^2}{2\sigma^2} + \mu \|Ww\|_1, \qquad (7)$$

where W is the framelet transform satisfying $W^T W = I$ with the identity matrix I.

We demonstrate the convexity of the proposed model (7) under certain mild conditions in the following, as discussed in [11].

Proposition 1 *If* $\alpha \geq \frac{(3-\inf f)\sqrt{6}}{9 \sup \sqrt{f}}$, *the model* (7) *is component-wise convex on* u.

Proof Let $E(u) = \langle \log u + \frac{f}{u}, 1 \rangle + \alpha \|\sqrt{u} - \sqrt{f}\|_2^2$. With $t \in \mathbb{R}^+$ and parameter α, we define a function g as

$$g(t) := \log t + \frac{f}{t} + \alpha(\sqrt{t} - \sqrt{f})^2.$$

We can get the second-order derivative differentiation of g as

$$g''(t) = -t^{-2} + 2ft^{-3} + \frac{\alpha\sqrt{f}}{2}t^{-\frac{3}{2}}.$$

Thus, when $\alpha \geq \frac{(3-\inf f)\sqrt{6}}{9 \sup \sqrt{f}}$, we have $g''(t) \geq 0$, i.e., g is convex. Furthermore, since function g has only one minimizer, g is strictly convex when $\alpha = \frac{(3-\inf f)\sqrt{6}}{9 \sup \sqrt{f}}$. Therefore, the function $\langle \log u + \frac{f}{u}, 1 \rangle + \alpha \|\sqrt{u} - \sqrt{f}\|_2^2 + \frac{\|Hw-u\|_2^2}{2\sigma^2}$ is strictly convex. Based on the convexity of the wavelet tight frame regularization, we conclude that the model (7) is convex. □

3 Algorithm and Convergence Analysis

This section proposes an iterative algorithm to solve the proposed model (7). The objective function in (7) is convex, and there are various optimization algorithms that can be applied to this problem, such as classical ADMM. Although the objective function of the proposed model can be split into two-block convex functions, solving the ADMM subproblems with high accuracy can be computationally expensive. To reduce the computational burden, one strategy is to divide the variables in (7) into three or more blocks based on their composite structures and solve the resulting problems using a multi-block ADMM type that directly extends the 2-block ADMM to a multi-block setup. However, this method of direct scaling may not converge, which can be a potential issue. Therefore, we propose an inexact sGS-imsPADMM algorithm to solve (7). This algorithm can reduce the cost of solving subproblems while ensuring theoretical convergence.

3.1 An Inexact sGS-imsPADMM with Relative Error Control for Solving (7)

By introducing an auxiliary variable x, we first reformulate the minimization problem (7) into an equivalent one as follows:

$$
\min_{u,w,x} \left\langle \log u + \frac{f}{u}, 1 \right\rangle + \alpha \left\| \sqrt{u} - \sqrt{f} \right\|_2^2 + \frac{\|Hw - u\|_2^2}{2\sigma^2} + \mu \|x\|_1,
$$
$$
\text{s.t.} \quad x - Ww = 0. \tag{8}
$$

Define $y_1 = u$, $y_2 = w$ and $y = (y_1, y_2)$, $x \in \mathcal{X}$ and $y \in \mathcal{Y}$, then problem (8) falls within the following general convex composite programming:

$$
\min_{x \in \mathcal{X}, y \in \mathcal{Y}} \mu \|x\|_1 + \frac{\|Hy_2 - y_1\|_2^2}{2\sigma^2} + \left\langle \log y_1 + \frac{f}{y_1}, 1 \right\rangle + \alpha \left\| \sqrt{y_1} - \sqrt{f} \right\|_2^2,
$$
$$
\text{s.t.} \quad x - Wy_2 = 0. \tag{9}
$$

Let us define $g(y) = g(y_1, y_2) := \frac{\|Hy_2 - y_1\|_2^2}{2\sigma^2}$. Then it is a continuously differentiable and convex function, and its gradient is Lipschitz continuous. Therefore, there exists a positive semidefinite matrix Σ_g such that for any y, $y' \in \mathcal{Y}$,

$$
g(y) \le \widehat{g}(y; y') := g(y') + \left\langle \nabla g(y'), y - y' \right\rangle + \frac{1}{2} \left\| y - y' \right\|_{\Sigma_g}^2. \tag{10}
$$

Define $p(x) := \mu \|x\|_1$ and $q(y) := \left\langle \log y_1 + \frac{f}{y_1}, 1 \right\rangle + \alpha \left\| \sqrt{y_1} - \sqrt{f} \right\|_2^2$, and it follows from Proposition 1 that both of them are closed proper convex functions when $\alpha \ge \frac{(3 - \inf f)\sqrt{6}}{9 \sup \sqrt{f}}$. For any $z := (x, y, l) \in \mathcal{X} \times \mathcal{Y} \times \mathcal{L}$ and $(x', y') \in \mathcal{X} \times \mathcal{Y}$, the majorized augmented Lagrangian function associated with (9) is

$$
L_\beta(x, y; (x', y', l)) = p(x) + q(y) + \widehat{g}(y; y') + \langle l, x - Wy_2 \rangle + \frac{\beta}{2} \|x - Wy_2\|_2^2, \tag{11}
$$

where β is the penalty parameter and l is the Lagrangian multiplier.

We say that the Slater constraint qualifying (CQ) holds for problem (9), if it satisfies

$$
\{(x, y) \mid x \in \mathrm{ri}(\mathrm{dom}\, p),\ y \in \mathrm{ri}(\mathrm{dom}\, q),\ x - Wy_2 = 0\} \ne \emptyset, \tag{12}
$$

where 'dom' represents the domain of definition, and 'ri' represents taking the open set of the domain of definition. When the Slater CQ is satisfied, according to Corollaries 28.2.2 and 28.3.1 in [29], the solution set of (9) is non-empty.

In the following, we propose an inexact sGS-imsPADMM with relative error control for solving the proposed model (7). The concrete algorithm framework is summarized in Algorithm 1.

Next, we explain how to solve these subproblems in Algorithm 1, respectively. For x-subproblem in Step 1, we have

$$
x^{k+1} = \arg\min_x L_\beta(x, y_1^k, y_2^k; z^k) + \frac{1}{2} \left\| x - x^k \right\|_{\mathcal{P}}^2. \tag{13}
$$

The above problem is equivalent to evaluating the proximal operator of the ℓ_1-norm function, which has a closed-form solution as follows:

$$
x^{k+1} = \mathcal{T}_{\mu/(\beta + \lambda_{\max}(\mathcal{P}))} \left(\frac{\beta W y_1^k - l^k + \mathcal{P} x^k}{\beta + \lambda_{\max}(\mathcal{P})} \right), \tag{14}
$$

Algorithm 1 An inexact sGS-imsPADMM with relative error control for solving (7).

Let $\vartheta \in (0, (1 + \sqrt{5})/2)$ be the step-length and $\{\varepsilon_k\}_{k \geq 0}$ be a nonnegative summable sequence satisfying $\sum_{k=0}^{\infty} \varepsilon_k^2 < +\infty$. Let $\mathcal{P}$ and $\widetilde{\mathcal{Q}} := \mathrm{Diag}(\widetilde{\mathcal{Q}}_1, \widetilde{\mathcal{Q}}_2)$ be given matrices which satisfy

$$\mathcal{P} \geq 0, \quad \mathcal{P} + \beta I^T I > 0; \quad \frac{1}{2}\Sigma_g + \widetilde{\mathcal{Q}} \geq 0, \quad \frac{1}{2}\Sigma_g + \widetilde{\mathcal{Q}} + \beta W^T W > 0.$$

For $k = 0, 1, 2, \ldots$, perform the following steps:
Step 1. Compute

$$x^{k+1} = \arg\min_{x} L_\beta\left(x, y^k; z^k\right) + \frac{1}{2}\left\|x - x^k\right\|_{\mathcal{P}}^2.$$

Step 2a. (Backward GS sweep) Compute

$$\widetilde{y}_2^{k+1} \approx \arg\min_{y_2} L_\beta\left(x^{k+1}, y_1^k, y_2; z^k\right) + \frac{1}{2}\left\|y_2 - y_2^k\right\|_{\widetilde{\mathcal{Q}}_2}^2,$$

$$\widetilde{\gamma}_2^{k+1} \in \partial_{y_2} L_\beta\left(x^{k+1}, y_1^k, \widetilde{y}_2^{k+1}; z^k\right) + \widetilde{\mathcal{Q}}_2\left(\widetilde{y}_2^{k+1} - y_2^k\right) \text{ with } \left\|\widetilde{\gamma}_2^{k+1}\right\| \leq \varepsilon_k \left\|y_2^k - y_2^{k-1}\right\|.$$

Step 2b. (Forward GS sweep) Compute

$$y_1^{k+1} \approx \arg\min_{y_1} L_\beta\left(x^{k+1}, y_1, \widetilde{y}_2^{k+1}; z^k\right) + \frac{1}{2}\left\|y_1 - y_1^k\right\|_{\widetilde{\mathcal{Q}}_1}^2,$$

$$\gamma_1^{k+1} \in \partial_{y_1} L_\beta\left(x^{k+1}, y_1^{k+1}, \widetilde{y}_2^{k+1}; z^k\right) + \widetilde{\mathcal{Q}}_1\left(y_1^{k+1} - y_1^k\right) \text{ with } \left\|\gamma_1^{k+1}\right\| \leq \varepsilon_k \left\|y_1^{k+1} - y_1^k\right\|.$$

$$y_2^{k+1} \approx \arg\min_{y_2} L_\beta\left(x^{k+1}, y_1^{k+1}, y_2; z^k\right) + \frac{1}{2}\left\|y_2 - y_2^k\right\|_{\widetilde{\mathcal{Q}}_2}^2,$$

$$\gamma_2^{k+1} \in \partial_{y_2} L_\beta\left(x^{k+1}, y_1^{k+1}, y_2^{k+1}; z^k\right) + \widetilde{\mathcal{Q}}_2\left(y_2^{k+1} - y_2^k\right) \text{ with } \left\|\gamma_2^{k+1}\right\| \leq \varepsilon_k \left\|y_2^{k+1} - y_2^k\right\|.$$

Step 3. Compute

$$l^{k+1} = l^k + \vartheta\beta\left(x^{k+1} - Wy_2^{k+1}\right).$$

For any $k \geq 0$, set $y^{k+1} := (y_1^{k+1}, y_2^{k+1})$ and the corresponding error vector $\gamma^{k+1} = (\gamma_1^{k+1}, \gamma_2^{k+1})$.

---

where $\lambda_{\max}(\mathcal{P})$ denotes the largest eigenvalue of the matrix $\mathcal{P}$ and the operator $\mathcal{T}_\sigma$ is a soft-thresholding operator defined as

$$(\mathcal{T}_\sigma(x))_i = \mathrm{sgn}(x_i)[|x_i| - \sigma]_+, \tag{15}$$

with $\mathrm{sgn}(\cdot)$ being a signum function and $[x_i]_+$ means $\max(x_i, 0)$.

The y_1-subproblem in Step 2b of Algorithm 1 can be read as

$$y_1^{k+1} \approx \arg\min_{y_1} L_\beta\left(x^{k+1}, y_1, \widetilde{y}_2^{k+1}; z^k\right) + \frac{1}{2}\left\|y_1 - y_1^k\right\|_{\widetilde{\mathcal{Q}}_1}^2, \tag{16}$$

which can be computed inexactly by Newton iterative method and then the corresponding error vector γ_1^{k+1} can be obtained.

The y_2-subproblem in Step 2b is equivalent to solving the following linear system:

$$\gamma_2^{k+1} \in \frac{H^T(Hy_2 - y_1^{k+1})}{\sigma^2} - \beta W^T\left(x^{k+1} - Wy_2 + \frac{l^k}{\beta}\right) + (\Sigma_g + \widetilde{\mathcal{Q}}_2)(y_2 - y_2^k). \tag{17}$$

Under the periodic boundary condition (BC) for y_1, and since $W^T W = I$, where I is identity matrix. We can use Fourier transform to compute the solution of (17).

3.2 Convergence Analysis

In this section, we first give the Karush-Kuhn-Tucker (KKT) condition, and prove the convergence of the simplified algorithm under the premise that the solution exists.

It follows from [29] that $(\bar{x}, \bar{y}) \in \mathcal{X} \times \mathcal{Y}$ is the solution of problem (9) if and only if there is a Lagrangian multiplier $\bar{l} \in \mathcal{L}$ of the augmented Lagrangian function for (9), such that $(\bar{x}, \bar{y}, \bar{l}) \in \mathcal{X} \times \mathcal{Y} \times \mathcal{L}$ is the solution of the following KKT conditions

$$0 \in \partial p(x) + l, \quad 0 \in \partial q(y) + \nabla g(y) - W^T l, \quad 0 = x - W y_2. \tag{18}$$

We denote $z := (x, y, l)$ and $\mathcal{Z} := \mathcal{X} \times \mathcal{Y} \times \mathcal{L}$, then the solution set of KKT system (18) for problem (9) is denoted by $\bar{\mathcal{Z}}$.

Let $\theta : \mathcal{V} \to (-\infty, +\infty]$ be a closed convex function, then the Moreau-Yosida proximal mapping $\Pi_\theta(v)$ related to θ is defined as

$$\Pi_\theta(v) := \arg\min_{v' \in \mathcal{V}} \left\{ \theta(v') + \frac{1}{2} \|v' - v\|^2 \right\}, \quad \forall v \in \mathcal{V}. \tag{19}$$

The Moreau-Yosida proximal map [17] is a globally Lipschitz, that is,

$$\|\Pi_\theta(v) - \Pi_\theta(v')\|^2 \le \langle v - v', \Pi_\theta(v) - \Pi_\theta(v') \rangle. \tag{20}$$

We define the KKT mapping $e(\cdot) : \mathcal{Z} \to \mathcal{Z}$ as

$$e(z) := \begin{pmatrix} x - \Pi_p(x - Il) \\ y - \Pi_q(y - (\nabla g(y) - W^T l)) \\ -x + W y_2 \end{pmatrix}, \quad \forall z \in \mathcal{Z}. \tag{21}$$

Note that there exists $z^* \in \bar{\mathcal{Z}}$ if and only if $e(z^*) = 0$.

Next, for the positive semidefinite matrix Σ_g, we use the following decomposition:

$$\begin{pmatrix} (\Sigma_g)_{11} & (\Sigma_g)_{12} \\ (\Sigma_g)_{12}^T & (\Sigma_g)_{22} \end{pmatrix}, \tag{22}$$

and define the matrices $\mathcal{M}$ and $\widetilde{\mathcal{N}}$ as follows:

$$\mathcal{M} := \mathcal{P} + \beta I^T I = \mathcal{P} + \beta I \quad \text{and} \quad \widetilde{\mathcal{N}} := \Sigma_g + \widetilde{\mathcal{Q}} + \beta W^T W = \Sigma_g + \widetilde{\mathcal{Q}} + \beta I. \tag{23}$$

Accordingly, we further define $\mathcal{N}_d := \mathrm{Diag}(\mathcal{N}_{11}, \mathcal{N}_{22})$, where $\mathcal{N}_{11} := \widetilde{\mathcal{Q}}_1 + (\Sigma_g)_{11}$ and $\mathcal{N}_{22} := \widetilde{\mathcal{Q}}_2 + (\Sigma_g)_{22} + \beta I$.

From the above definitions, we have

$$\widetilde{\mathcal{N}} = \begin{pmatrix} \mathcal{N}_{11} & \frac{1}{2}(\Sigma_g)_{12} \\ \frac{1}{2}(\Sigma_g)_{12}^T & \mathcal{N}_{22} \end{pmatrix} = \mathcal{N}_d + \mathcal{N}_r + \mathcal{N}_r^T, \tag{24}$$

where $\mathcal{N}_r$ is the strictly upper triangular part of $\widetilde{\mathcal{N}}$. Moreover, we define the following matrices:

$$\mathcal{Q} := \widetilde{\mathcal{Q}} + \mathrm{sGS}(\widetilde{\mathcal{N}}), \quad \mathcal{N} := \Sigma_g + \mathcal{Q} + \beta I = \widetilde{\mathcal{N}} + \mathrm{sGS}(\widetilde{\mathcal{N}}), \tag{25}$$

where $\mathrm{sGS}(\mathcal{N}) := \mathcal{N}_r \mathcal{N}_d^{-1} \mathcal{N}_r^T$. Denote $d_y^{k+1} := \gamma^{k+1} + \mathcal{N}_r \mathcal{N}_d^{-1}(\gamma^{k+1} - \widetilde{\gamma}^{k+1})$. Then we have the following proposition.

Proposition 2 *The sequences $\{(x^k, y^k, l^k)\}$, $\{\gamma^k\}$ and $\{\widetilde{\gamma}^k\}$ generated by the sGS-imsPADMM are well-defined. For any $k \ge 0$, d_y^{k+1} satisfy*

$$\left\| d_y^{k+1} \right\|_{\mathcal{N}^{-1}}^2 \le c' \varepsilon_k^2 \left(\left\| y^k - y^{k-1} \right\|_{\mathcal{N}}^2 + \left\| y^{k+1} - y^k \right\|_{\mathcal{N}}^2 \right), \tag{26}$$

where c' is defined as

$$c' := \left(4 \left\| \mathcal{N}_d^{-\frac{1}{2}} \right\|^2 + 2 \left\| \mathcal{N}_d^{-\frac{1}{2}} (\mathcal{N}_d + \mathcal{N}_r)^{-1} \right\|^2 \right) \Big/ \lambda_{\min}^2 \mathcal{N} > 0. \tag{27}$$

Proof According to the sGS decomposition theorem ([8], Proposition 4.1 and [21], Theorem 1), Proposition 4.1 [9] and Proposition 2 [19], we can readily show that the sequences are well-defined and that (26) holds.   □

We define the mapping $\mathcal{R} : \mathcal{X} \times \mathcal{Y}$ by $\mathcal{R}(x, y) := x - W y_1$, $\forall (x, y) \in \mathcal{X} \times \mathcal{Y}$, and introduce some notations in the following, for $k \geq 0$,

$$\Delta_x^k := x^k - x^{k+1}, \quad \Delta_y^k := y^k - y^{k+1}, \quad r^k := \mathcal{R}\left(x^k, y^k\right), \quad \tilde{l}^{k+1} := l^k + \beta r^{k+1}, \tag{28}$$

with the convention that $\bar{y}^0 = y^0$.

Lemma 1 *[8, Lemma 5.1] Let $\{a_k\}_{k \geq 0}$ be a nonnegative sequence satisfying $a_{k+1} \leq a_k + \varepsilon_k$ for all $k \geq 0$, where $\{\varepsilon_k\}_{k \geq 0}$ is a nonnegative and summable sequence of real numbers. Then the quasi-Fejér monotone sequence $\{a_k\}$ converges to a unique limit point.*

In order to illustrate the relationship between the terms $\left\| z^{k+1} - z^k \right\|$, $\left\| z^k - z^{k-1} \right\|$ and $\left\| e(z^{k+1}) \right\|$, we give the following two lemmas, whose proofs are similar to those in [9, 19] and [39], respectively.

Lemma 2 *Let $\{z^k\}$ be the sequence generated by the sGS-imsPADMM. For any $k \geq 1$, we have*

$$\left\| e(z^{k+1}) \right\|^2 \leq \left\| z^{k+1} - z^k \right\|_{\mathcal{K}_1}^2 + \left\| z^k - z^{k-1} \right\|_{\mathcal{K}_2}^2, \tag{29}$$

where

$$\mathcal{K}_1 := c_1 \mathrm{Diag}(I, I + \beta I, (\vartheta^2 \beta)^{-1} I), \qquad \mathcal{K}_2 := c_2 \mathrm{Diag}(I, I, 0),$$

$$\begin{cases} c_1 := \max\{c_1^1, c_1^2, c_1^3\}, \\ c_1^1 := 8 \left(\lambda_{\max}(\mathcal{P} + \beta I) \right)^2, \\ c_1^2 := \max \left\{ 6 \left(\lambda_{\max}\left(\frac{1}{2} \Sigma_g + \mathcal{Q} + \beta I \right) + \frac{1}{2} \lambda_{\max}(\Sigma_g) \right)^2, 4\beta I \right\}, \\ c_1^3 := \beta^{-1} + 7(1 - \vartheta)^2 \beta I, \end{cases}$$

and

$$\begin{cases} c_2 := \max\{c_2^1, c_2^2\}, \\ c_2^1 := 4 \max_k \{\epsilon_k^2\} \left(\lambda_{\max}(\mathcal{P} + \beta I) \right)^2, \\ c_2^2 := 3 \max_k \{\epsilon_k^2\} \left(\lambda_{\max}\left(\frac{1}{2} \Sigma_g + \mathcal{Q} + \beta I \right) + \frac{1}{2} \lambda_{\max}(\Sigma_g) \right)^2. \end{cases}$$

Lemma 3 *Let $e : \mathcal{X} \to (-\infty, +\infty)$ be a smooth convex function and assume that there exists a self-adjoint positive semidefinite linear operator $\mathcal{P}$ such that, for any given $x' \in \mathcal{X}$,*

$$e(x) \leq e(x') + \left\langle \nabla e(x'), x - x' \right\rangle + \frac{1}{2} \left\| x - x' \right\|_{\mathcal{P}}^2. \tag{30}$$

Then, for any $x_1, x_2 \in \mathcal{X}$, we obtain

$$\left\langle \nabla e(x_1) - \nabla e(x'), x_2 - x' \right\rangle \geq -\frac{1}{4} \|x_1 - x_2\|_{\mathcal{P}}^2. \tag{31}$$

For any $k \geq 1$, we define for any $z \in \mathcal{Z}$ and $k \geq 0$,

$$
\begin{aligned}
\phi_k(z) :=& \frac{1}{\vartheta\beta} \left\| l - l^k \right\|^2 + \left\| x - x^k \right\|_{\mathcal{P}}^2 + \left\| y - y^k \right\|_{\mathcal{N}}^2 \\
& + (1+\nu) \left\| y^k - y^{k-1} \right\|_{\Sigma_g + \mathcal{Q} + \frac{\nu\beta}{1+\nu}I}^2.
\end{aligned} \tag{32}
$$

The following proposition is essential for establishing the convergence.

Proposition 3 *Suppose that the solution set $\bar{\mathcal{Z}}$ to the KKT system of problem (9) is nonempty. Let $\{z_k\}$ be the sequence generated by the sGS-imsPADMM with relative error control. Then, for any $\bar{z} := (\bar{x}, \bar{y}, \bar{l}) \in \bar{\mathcal{Z}}$, $k \geq 1$ and $\nu > 0$,*

$$
\begin{aligned}
& \left\| \triangle_x^k \right\|_{\mathcal{P}}^2 + \left\| \triangle_y^k \right\|_{\mathcal{O}}^2 - 2\nu \left(\left\| \triangle_x^k \right\|_{\mathcal{M}}^2 + \left\| \triangle_y^k \right\|_{\mathcal{N}}^2 \right) + \widehat{\omega} \left\| r^{k+1} \right\|^2 \\
& \leq \phi_k(\bar{z}) - \left(1 - \frac{\epsilon_k^2}{\nu} \right) \phi_{k+1}(\bar{z}) + \omega \left\| r^k \right\|^2 - \left(1 - \frac{\epsilon_k^2}{\nu} \right) \omega \left\| r^{k+1} \right\|^2 \\
& \quad - \frac{\epsilon_k^2}{\nu} \left\| x^{k+1} - \bar{x} \right\|_{\mathcal{P}}^2,
\end{aligned} \tag{33}
$$

where $\omega := \beta(1 - \min\{\vartheta, \vartheta^{-1}\})$, $\widehat{\omega} := \beta(1 - \vartheta + \min\{\vartheta, \vartheta^{-1}\})$ and $\mathcal{O} := \frac{1}{2}\Sigma_g + \mathcal{Q} + \widehat{\omega}\vartheta I$.

Proof The proof of Proposition 3 is detailed in the Appendix A.1. □

Now we present the convergence result of the proposed sGS-imsPADMM in the following.

Theorem 1 *Suppose that the solution set $\bar{\mathcal{Z}}$ to the KKT system of problem (7) is nonempty and $\{z_k\}$ is generated by the sGS-imsPADMM. Assume that*

$$\mathcal{M} = \mathcal{P} + \beta I > 0 \quad and \quad \mathcal{G} := \Sigma_g + \mathcal{Q} + \frac{\nu\beta}{1+\nu}I > 0. \tag{34}$$

Then, we get the sequence $\{z_k\}$ converges to a point in $\bar{\mathcal{Z}}$.

Proof The proof of Theorem 1 is detailed in the Appendix 1. □

4 Numerical Experiments

In this section, to demonstrate the effectiveness of the proposed model/method, we compared our model/method with other models/methods: the DZ model [11], the HNZ model [14], the FL model [18], the EM-CNN method [36], and the PARM model [24]. All the experiments have been successfully tested in MATLAB R2019b (Windows 10) and were run on a PC with Intel(R) Core(TM) i5-6200U CPU @2.30 GHz and 8 GB of RAM.

In our experiments, the quality of the recovered images is measured quantitatively by the peak signal noise ratio (PSNR) and the structural similarity index measure (SSIM) [37]. Note

Table 1 Explanation of symbols for blur with mixed noise

Symbol	Blur	σ	K	Symbol	Blur	σ	K
MB1	MB(9,30)	1	100	GB1	GB(5,2)	1	100
MB2	MB(15,60)	5	50	GB2	GB(9,4)	5	50
MB3	MB(10,120)	10	30	GB3	GB(9,4)	10	30

that larger PSNR and larger SSIM values mean better restored results. If the image size is $m \times n$, then PSNR is defined as follows:

$$\text{PSNR} = 10 \log \frac{mn \max(\max(\hat{y_2}), \max(y_2))^2}{\|\hat{y_2} - y_2\|^2}, \tag{35}$$

where $\hat{y_2}$ and y_2 are the restored image and the original image, respectively. Based on the KKT mapping (21), the iteration for our models is terminated when the following condition is met [8]:

$$\|e(z^{k+1})\| < 10^{-4}. \tag{36}$$

4.1 Parameter Setting

For all these methods, we adjust the parameters within a specific range to achieve the best PSNR values and visually the best-restored images. For our model, we select the regularization parameter α in the range [3, 9], λ in the range [0.01, 0.04] and μ in the range [1, 1.8]. In addition, Fig. 2 displays the restoration results obtained by our model under the MB1 (the symbol is presented in Table 1) with different values of parameters. The step-length ϑ is set to be $\vartheta = 1.618 \in (0, (1 + \sqrt{5})/2)$ for guaranteed convergence, and the sequence $\{\varepsilon_k\}$ that we used is chosen such that $\varepsilon_k \leq 1/k$.

In this experiment, six images (all of the size 256×256) are given in Fig. 1 to test the performance of the proposed model. To generate the observed images, the test images are contaminated with different blurring motion blur (MB) and Gaussian blur (GB), different standard deviations σ=1, 5 and 10 for Gaussian noise and different shape parameters K=30, 50 and 100 for Gamma noise. The larger σ is, the more serious the additive Gaussian noise is. On the contrary, the smaller K is, the more serious the multiplicative Gamma noise is. For MB, we use `len` = 9, 10 and 15 with an `angle` of 30, 60 and 120, where `len` represents the motion translation length of motion blur, `angle` represents the angle of motion rotation. As for GB, the blurring kernels to be tested are of size 5×5 and 9×9. Then, the standard deviations in GB are set as 2 and 4. Furthermore, we use the notation of MB(9,30) to denote the case of motion blur of `len` = 9 with an `angle` of 30. Similarly, GB(5,2) will be set for a Gaussian kernel of size 5×5 and a standard deviation of 2. Specifically, we define the symbol MB1 to be MB(9,30) with additive Gaussian noise of standard deviation of $\sigma = 1$ and multiplicative Gamma noise of $K = 100$. In the same way, we define the symbol GB2 to be GB(9,4) with additive Gaussian noise of standard deviation of $\sigma = 5$ and multiplicative Gamma noise of $K = 50$. All the symbols are presented in Table 1.

4.2 Comparison with Other Models

In order to reflect the role of the quadratic penalty in the proposed model, we first compare the results without the penalty. The model without quadratic penalty is reduced to
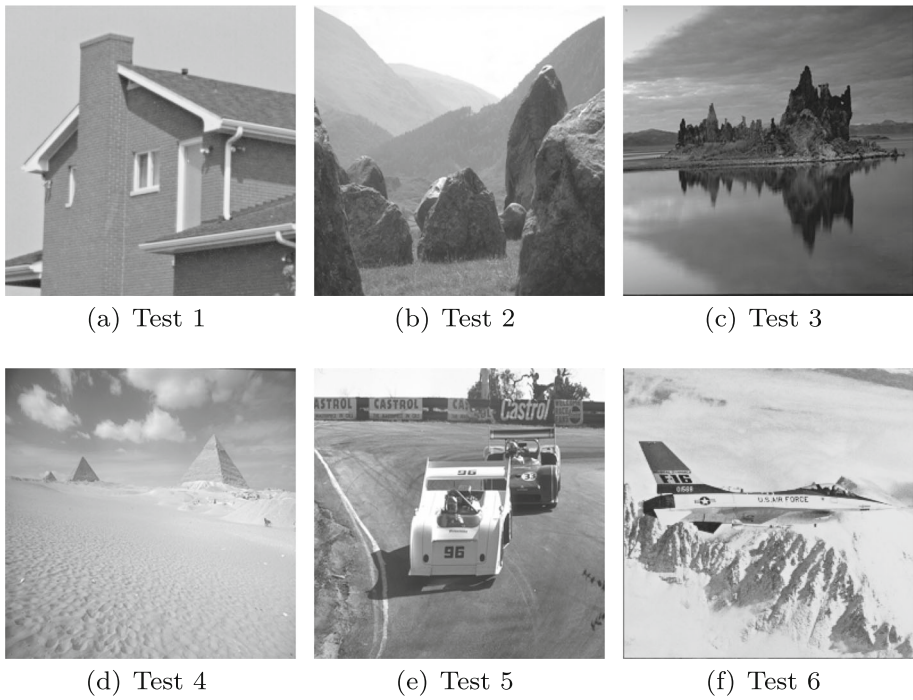
(a) Test 1   (b) Test 2   (c) Test 3

(d) Test 4   (e) Test 5   (f) Test 6

Fig. 1 Standard test images

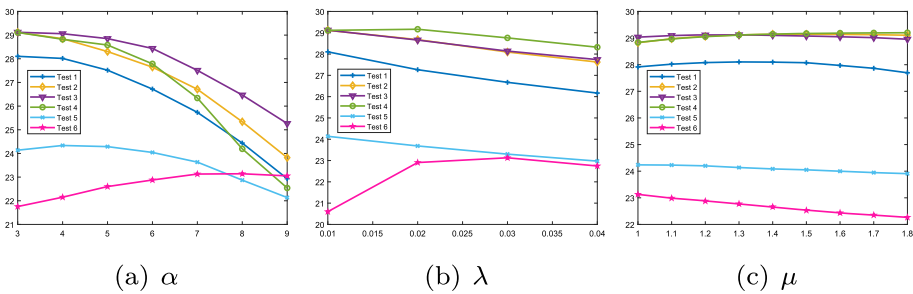(a) α (b) λ (c) μ

Fig. 2 Plots of PSNR(dB) value versus every parameter in our model for different test images at MB1

$$\min_{u>0,w} \left\langle \log u + \frac{f}{u}, 1 \right\rangle + \frac{\|Hw - u\|_2^2}{2\sigma^2} + \mu\|Ww\|_1. \tag{37}$$

Figure 3 shows the comparison results of the simplified model and the proposed model. It can be observed from the image that the model without penalty term performs poorly in denoising. This example demonstrates the importance of penalty.

Next, we compare the recovery results of the simple approach with a common least-square term $\|u - f\|_2^2$ (denoted as Mod. 1). The model can be formulated as

$$\min_{u>0,w} \left\langle \log u + \frac{f}{u}, 1 \right\rangle + \alpha\|u - f\|_2^2 + \frac{\|Hw - u\|_2^2}{2\sigma^2} + \mu\|Ww\|_1. \tag{38}$$
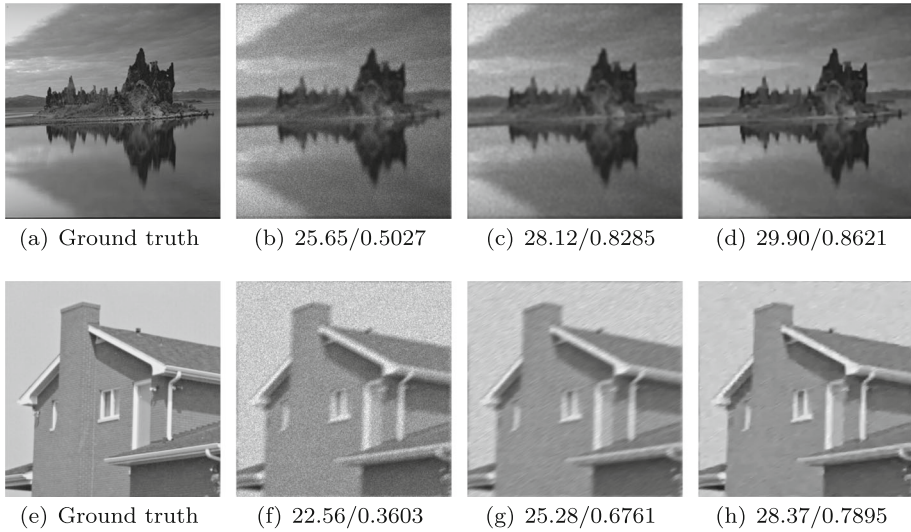
| (a) Ground truth | (b) 25.65/0.5027 | (c) 28.12/0.8285 | (d) 29.90/0.8621 |

| (e) Ground truth | (f) 22.56/0.3603 | (g) 25.28/0.6761 | (h) 28.37/0.7895 |

Fig. 3 Comparison of simplified model for image restoration effect and PSNR(dB)/SSIM values, respectively. **a** and **e** are ground truth; **b** and **f** are the images degraded with GB1 and MB1, respectively; **c** and **g** are the images degradation results of the simplified model; **d** and **h** are the images degradation results of ours

According to Proposition 1, we can conclude, if $\alpha \geq \frac{1}{54f^2}$, the model (38) is component-wise convex on u. In addition, the image restoration effect is shown in Sect. 4.3. It can be found from the numerical results in Table 2 and Table 3 that the image degradation becomes more serious, the restoration effect of the Mod. 1 decreases more. The Mod. 1 is less robust.

To demonstrate that our tightframe-based model is influential, we present the comparison with the TV-based model (denoted as TV model). The TV-based model can be formulated as

$$\min_{u>0,w} \left\langle \log u + \frac{f}{u}, 1 \right\rangle + \alpha \left\| \sqrt{u} - \sqrt{f} \right\|_2^2 + \frac{\|Hw - u\|_2^2}{2\sigma^2} + \mu_1 \|\nabla w\|_1. \quad (39)$$

We use the sGS-imsPADMM method to solve (39). In order to apply sGS-imsPADMM, we express the minimization problem (39) as an equivalent form:

$$\min_{u,w,c} \left\langle \log u + \frac{f}{u}, 1 \right\rangle + \alpha \left\| \sqrt{u} - \sqrt{f} \right\|_2^2 + \frac{\|Hw - u\|_2^2}{2\sigma^2} + \mu_1 \|c\|_1,$$
$$\text{s.t.} \quad c - \nabla w = 0. \quad (40)$$

Let $y_1 = u$, $y_2 = w$ and $y = (y_1, y_2)$, $c \in \mathcal{C}$ and $y \in \mathcal{Y}$, when $\alpha \geq \frac{(3 - \inf f)\sqrt{6}}{9 \sup \sqrt{f}}$, according to Sect. 3, for any $h := (c, y, p) \in \mathcal{C} \times \mathcal{Y} \times \mathcal{P}$ and $(c', y') \in \mathcal{C} \times \mathcal{Y}$. There exists a positive semidefinite matrix Σ_h such that for $y, y' \in \mathcal{Y}$,

$$g(y) \leq \hat{g}(y; y') := g(y') + \left\langle \nabla g(y'), y - y' \right\rangle + \frac{1}{2} \left\| y - y' \right\|_{\Sigma_h}^2. \quad (41)$$

The majorized augmented Lagrangian function is given by

$$L_\tau(c, y; (c', y', p)) = \mu \|c\|_1 + q(y) + \hat{g}(y; y') + \langle p, c - \nabla w \rangle + \frac{\tau}{2} \|c - \nabla w\|_2^2, \quad (42)$$

Table 2 PSNR (dB), SSIM for motion blur with different noise levels

Images	Methods	PSNR			SSIM		
		MB1	MB2	MB3	MB1	MB2	MB3
Test 1	DZ	25.69	23.07	24.94	0.7413	0.6712	0.6983
	HNZ	27.47	24.33	24.20	0.7872	0.6893	0.7310
	FL	27.12	25.09	25.39	0.7262	0.6957	0.6864
	EM-CNN	25.33	23.73	24.52	0.7052	0.6095	0.5981
	PARM	26.19	23.15	25.03	0.7731	0.6886	0.6923
	TV	28.19	25.57	25.67	0.7508	0.7011	0.6674
	Mod. 1	27.19	23.45	18.76	0.7721	0.5463	0.2642
	Ours	**28.37**	**25.74**	**25.85**	**0.7895**	**0.7194**	**0.7493**
Test 2	DZ	27.36	24.51	25.16	0.7341	0.7035	0.6580
	HNZ	27.20	24.04	23.08	0.7812	0.7456	0.7425
	FL	27.66	26.03	25.45	0.7252	0.7285	0.6977
	EM-CNN	26.99	25.13	24.80	0.7609	0.6902	0.6543
	PARM	27.30	24.39	24.71	0.7806	0.7400	0.6589
	TV	27.60	26.34	25.79	0.7701	0.7440	0.7219
	Mod. 1	27.91	24.54	18.62	0.7666	0.5912	0.2667
	Ours	**29.26**	**26.96**	**26.20**	**0.8012**	**0.7606**	**0.7458**
Test 3	DZ	27.05	25.76	26.28	0.8165	0.7682	0.7571
	HNZ	28.78	26.98	26.82	0.4789	0.7914	0.7426
	FL	28.17	26.83	26.76	0.7575	0.7699	0.7740
	EM-CNN	26.82	25.35	26.06	0.7981	0.7169	0.6908
	PARM	27.48	26.04	26.43	0.8226	0.7688	0.7241
	TV	28.61	**26.98**	**26.95**	0.8378	0.7951	0.7854
	Mod. 1	27.89	25.80	21.55	0.8285	0.6450	0.3335
	Ours	**29.17**	26.95	26.48	**0.8544**	**0.7964**	**0.8017**
Test 4	DZ	28.90	27.31	27.91	0.6965	0.6613	0.6473
	HNZ	**29.22**	27.45	24.76	**0.7176**	0.6598	0.5271
	FL	28.51	27.16	26.85	0.6687	0.6518	0.6290
	EM-CNN	28.32	26.92	27.11	0.6417	0.5624	0.5515
	PARM	28.92	27.85	28.06	0.6959	0.6719	0.6643
	TV	29.05	27.89	27.95	0.6984	0.6723	0.6776
	Mod. 1	28.96	25.66	18.24	0.7160	0.4429	0.1815
	Ours	29.07	**28.13**	**28.09**	0.6950	**0.6775**	**0.6841**
Test 5	DZ	22.44	20.32	21.57	0.6173	0.5164	0.5689
	HNZ	23.42	21.47	21.34	0.6684	0.5792	0.5912
	FL	24.04	22.28	22.51	0.6173	0.5963	0.6165
	EM-CNN	22.35	20.15	21.40	0.6119	0.4854	0.5350
	PARM	22.48	20.29	21.59	0.6281	0.5255	0.5774
	TV	24.08	22.14	22.63	0.6986	0.5996	0.6206

Table 2 continued

Images	Methods	PSNR			SSIM		
		MB1	MB2	MB3	MB1	MB2	MB3
	Mod. 1	23.50	21.37	18.47	0.6675	0.4876	0.3217
	Ours	**24.46**	**22.46**	**22.70**	**0.7034**	**0.6057**	**0.6268**
Test 6	DZ	21.82	19.79	21.01	0.6680	0.5973	0.5631
	HNZ	22.41	20.35	19.57	0.6066	0.5981	0.4857
	FL	22.68	20.95	21.17	0.6754	0.6369	0.6004
	EM-CNN	21.20	19.96	20.76	0.5998	0.4875	0.4918
	PARM	21.88	20.26	21.03	0.6888	0.6207	0.6334
	TV	22.98	21.28	21.66	0.6151	0.6161	**0.6504**
	Mod. 1	22.64	20.59	16.46	0.6261	0.3863	0.2271
	Ours	**23.21**	**21.46**	**21.74**	**0.6932**	**0.6433**	0.6353
Average	DZ	25.54	23.46	24.48	0.7123	0.6530	0.6487
	HNZ	26.42	24.10	23.30	0.6733	0.6772	0.6366
	FL	26.36	24.72	24.68	0.6951	0.6799	0.6673
	EM-CNN	25.17	23.54	24.11	0.6863	0.5920	0.5869
	PARM	25.71	23.66	24.48	0.7315	0.6693	0.6584
	TV	26.75	25.03	25.11	0.7285	0.6880	0.6872
	Mod. 1	26.35	23.57	18.68	0.7295	0.5166	0.2658
	Ours	**27.26**	**25.28**	**25.18**	**0.7561**	**0.7005**	**0.7067**

In the last line of the table, we compute the average values

where τ is the penalty parameter and p is the Lagrangian multiplier. The sGS-imsADMM algorithm with a relative error criterion for solving (42) is presented in Algorithm 2. The image restoration effect is shown in Subsection 4.3.

4.3 Image Restoration Results Under Mixed Noise with Motion Blur

Figure 4 presents the visual effects of image degradation by additive noise, multiplicative noise, Gaussian blur, motion blur, and mixed noise with blur. It can be seen that multiplicative noise destroys the amount of image information, so the destruction of image information with blur and mixed noise is more serious. Therefore, we compare our models with some multiplicative noise models to show the superiority of the proposed models in removing mixed noise and blur. In Fig. 4, "Test 1" is degraded by Gaussian noise, Gamma noise and motion blur, respectively. (a)–(c) show the visual effects of different degraded images, (d) shows the image degraded by MB2. Similarly, (e)–(g) show the degradation of "Test 2" by Gaussian noise, Gamma noise and Gaussian blur, respectively. (h) shows the image degraded by GB3, and image degradation in (d) and (h) are the most serious. Image restoration in this case is even more difficult.

Table 2 shows the numerical results of the restored images by different methods. The best results in each case are highlighted in bold. It can be seen that our model achieves best data results in most cases under different degradation levels. In addition, our model gets a satisfactory result in terms of average values of SSIM and PSNR.

In order to more clearly demonstrate the advantages of our model, we present the visual effects of image restoration at a lower level of image degradation. We also display the zoomed

Table 3 PSNR (dB), SSIM for Gaussian blur with different noise levels

Images	Methods	PSNR			SSIM		
		GB1	GB2	GB3	GB1	GB2	GB3
Test 1	DZ	27.69	24.45	24.31	0.7741	0.6569	0.6811
	HNZ	28.87	25.46	25.17	0.8039	0.7312	0.6923
	FL	28.09	25.53	24.70	0.7606	0.7354	0.7169
	EM-CNN	27.31	23.73	23.75	0.7410	0.6095	0.5805
	PARM	28.08	24.73	24.41	0.8022	0.7229	0.6754
	TV	28.91	25.97	25.20	0.7609	0.7234	0.7101
	Mod. 1	29.02	25.35	21.73	0.7939	0.6656	0.4042
	Ours	**29.45**	**26.51**	**25.39**	**0.8040**	**0.7508**	**0.7375**
Test 2	DZ	27.76	25.34	25.20	0.7459	0.6333	0.6494
	HNZ	28.14	25.99	24.82	**0.7945**	0.7444	0.7058
	FL	28.16	26.27	25.57	0.7704	0.7438	0.7282
	EM-CNN	27.46	25.13	24.86	0.7784	0.6902	0.6420
	PARM	27.70	25.54	24.81	0.7922	0.7474	0.6461
	TV	28.22	26.46	25.82	0.7770	0.7568	0.7365
	Mod. 1	28.29	25.97	21.73	0.7827	0.6767	0.4154
	Ours	**29.46**	**27.10**	**25.93**	0.7910	**0.7574**	**0.7458**
Test 3	DZ	28.16	26.41	25.84	0.8373	0.7554	0.7425
	HNZ	29.65	27.14	**26.83**	0.8510	0.7969	0.7761
	FL	28.95	26.99	26.44	0.8048	0.7901	0.7837
	EM-CNN	28.09	25.82	25.55	0.8221	0.7288	0.6749
	PARM	28.70	26.57	25.95	0.8437	0.7810	0.7077
	TV	29.21	27.11	26.56	0.8179	0.7931	0.7829
	Mod. 1	28.86	26.53	23.67	0.8462	0.7639	0.5043
	Ours	**29.90**	**27.11**	25.89	**0.8621**	**0.7989**	**0.7857**
Test 4	DZ	29.49	27.67	27.66	0.7113	0.6195	0.6373
	HNZ	29.69	28.21	27.33	0.7288	0.6799	0.6332
	FL	29.10	27.58	27.08	0.6930	0.6687	0.6615
	EM-CNN	28.96	27.36	26.92	0.6596	0.5648	0.5390
	PARM	29.39	28.32	**27.74**	0.7048	0.6781	0.6519
	TV	29.39	28.26	27.56	0.7101	0.6814	0.6278
	Mod. 1	29.41	27.31	21.77	0.7148	0.6090	0.3146
	Ours	**29.69**	**28.41**	**27.74**	**0.7325**	**0.6849**	**0.6726**
Test 5	DZ	23.64	21.25	21.10	0.6687	0.5380	0.5360
	HNZ	24.64	22.12	21.82	0.7134	0.5970	0.5822
	FL	25.00	22.41	21.83	0.7247	0.6144	0.5850
	EM-CNN	23.67	21.11	20.93	0.6707	0.5203	0.4966
	PARM	23.59	21.30	21.10	0.6722	0.5641	0.5398

Table 3 continued

Images	Methods	PSNR			SSIM		
		GB1	GB2	GB3	GB1	GB2	GB3
	TV	25.06	22.29	21.76	0.7372	0.6079	0.5787
	Mod. 1	24.84	22.16	20.31	0.7203	0.5642	0.4193
	Ours	**25.35**	**22.62**	**22.08**	**0.7438**	**0.6172**	**0.5963**
Test 6	DZ	22.69	20.64	20.63	0.7089	0.4916	0.5385
	HNZ	22.99	20.69	20.52	0.7427	0.6242	0.5853
	FL	23.37	20.80	20.19	0.7221	0.6402	0.6209
	EM-CNN	22.37	20.51	20.41	0.6499	0.4950	0.4653
	PARM	22.75	20.81	20.65	0.7231	0.6275	0.6047
	TV	23.66	21.01	20.43	0.7171	0.6391	0.6094
	Mod. 1	23.60	21.19	18.85	0.6608	0.5015	0.3132
	Ours	**23.74**	**21.39**	**21.09**	**0.7619**	**0.6425**	**0.6226**
Average	DZ	26.57	24.29	24.12	0.7410	0.6158	0.6308
	HNZ	27.33	24.94	24.42	0.7724	0.6956	0.6625
	FL	27.11	24.93	24.30	0.7459	0.6988	0.6827
	EM-CNN	26.31	23.94	23.74	0.7203	0.6014	0.5664
	PARM	26.70	24.55	24.11	0.7564	0.6868	0.6376
	TV	27.41	25.18	24.56	0.7534	0.7003	0.6742
	Mod. 1	27.34	24.75	21.34	0.7531	0.6302	0.3952
	Ours	**27.93**	**25.52**	**24.69**	**0.7825**	**0.7086**	**0.6934**

In the last line of the table, we compute the average values

(a) 33.96/0.8359   (b) 22.02/0.3977   (c) 22.58/0.6959   (d) 19.40/0.2030

(e) 28.48/0.6110   (f) 20.95/0.3684   (g) 25.63/0.7600   (h) 19.09/0.1739
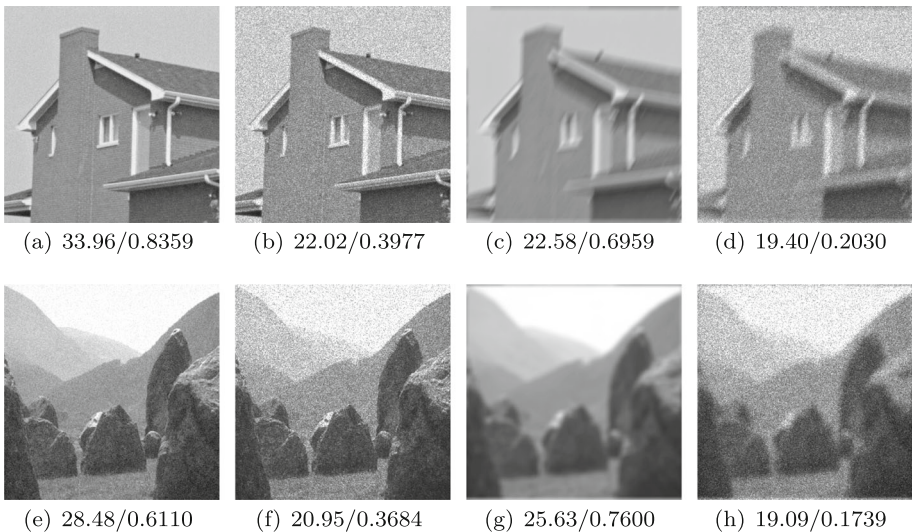
Fig. 4 Images degradation results and PSNR(dB)/SSIM values. **a** and **e** are the images degraded by Gaussian noise $\sigma = 5$ and 10, respectively; **b** and **f** are the images degraded by Gamma noise $K = 50$ and 30, respectively; **c** and **g** are the images degraded by blurring MB(15, 60) and GB(9, 4), respectively; **d** and **h** are the images degraded by MB2, GB3, respectively

---

Algorithm 2 Inexact sGS-imsPADMM for solving (39).

Let $\xi \in (0, (1 + \sqrt{5})/2)$ be the step-length and $\{\rho_k\}_{k \geq 0}$ be a summable sequence of nonnegative numbers satisfying $\sum_{k=0}^{\infty} \rho_k^2 < +\infty$. Let $\mathcal{S}$ and $\mathcal{T} := \mathrm{Diag}(\mathcal{T}_1, \mathcal{T}_2)$ be given matrix, we have

$$\mathcal{S} \geq 0, \quad \mathcal{S} + \tau I^T I > 0; \quad \frac{1}{2}\Sigma_h + \mathcal{T} \geq 0, \quad \frac{1}{2}\Sigma_h + \mathcal{T} + \tau \nabla^T \nabla > 0.$$

For $k = 0, 1, 2, ...$, perform the following steps:

Step 1. Compute

$$c^{k+1} = \arg\min_{c} L_\tau\left(c, y^k; h^k\right) + \frac{1}{2}\left\|c - c^k\right\|_{\mathcal{S}}^2.$$

Step 2a. (Backward GS sweep) Compute

$$\widetilde{y}_2^{k+1} \approx \arg\min_{y_2} L_\tau\left(x^{k+1}, y_1^k, y_2; h^k\right) + \frac{1}{2}\left\|y_2 - y_2^k\right\|_{\mathcal{T}_2}^2,$$

$$\widetilde{\delta}_2^{k+1} \in \partial_{y_2} L_\tau\left(x^{k+1}, y_1^k, \widetilde{y}_2^{k+1}; h^k\right) + \mathcal{T}_2\left(\widetilde{y}_2^{k+1} - y_2^k\right) \text{ with } \left\|\widetilde{\delta}_2^{k+1}\right\| \leq \rho_k\left\|y_2^k - y_2^{k-1}\right\|.$$

Step 2b. (Forward GS sweep) Compute

$$y_1^{k+1} \approx \arg\min_{y_1} L_\tau\left(x^{k+1}, y_1, \widetilde{y}_2^{k+1}; h^k\right) + \frac{1}{2}\left\|y_1 - y_1^k\right\|_{\mathcal{T}_1}^2,$$

$$\delta_1^{k+1} \in \partial_{y_1} L_\tau\left(x^{k+1}, y_1^{k+1}, \widetilde{y}_2^{k+1}; h^k\right) + \mathcal{T}_1\left(y_1^{k+1} - y_1^k\right) \text{ with } \left\|\delta_1^{k+1}\right\| \leq \rho_k\left\|y_1^{k+1} - y_1^k\right\|.$$

$$y_2^{k+1} \approx \arg\min_{y_2} L_\tau\left(x^{k+1}, y_1^{k+1}, y_2; h^k\right) + \frac{1}{2}\left\|y_2 - y_2^k\right\|_{\mathcal{T}_2}^2,$$

$$\delta_2^{k+1} \in \partial_{y_2} L_\tau\left(x^{k+1}, y_1^{k+1}, y_2^{k+1}; h^k\right) + \widetilde{\mathcal{Q}}_2\left(y_2^{k+1} - y_2^k\right) \text{ with } \left\|\delta_2^{k+1}\right\| \leq \rho_k\left\|y_2^{k+1} - y_2^k\right\|.$$

Step 3. Compute

$$p^{k+1} = p^k + \xi\tau\left(c^{k+1} - \nabla W\right).$$

For any $k \geq 0$, set $y^{k+1} := (y_1^{k+1}, y_2^{k+1})$ and the corresponding error vector $\delta^{k+1} = (\delta_1^{k+1}, \delta_2^{k+1})$.

---

regions of the restoration results in Figs. 5 and 6. It can be seen that the images recovered by our methods achieve the best quality concerning mixed noise removal and deblurring simultaneously. In Fig. 5, we observe that the DZ method [11], the HNZ model [14], the EM-CNN method [36], and the PARM method [24] can not completely remove the blur. Note that the FL method [18] and TV method results still have some motion blur in the red and green zoomed areas. There is still a lot of noise in the recovery results of the Mod. 1. The results of our model in these two aspects are satisfactory. A similar situation is shown in Fig. 6, the restoration results of the FL method and TV method in red enlarged areas can not remove the blur completely, where the number "96" is indistinct in the middle as if linked together. Moreover, it seems that the TV method results in stair-casing artifacts. Essentially, the traditional TV regularization will cause the stair-casing effect in the smooth area of the reconstructed image, and the texture information of the image can not be retained well.

4.4 Image Restoration Results Under Mixed Noise with Gaussian Blur

In this experiment, we degrade the standard test images Fig. 1 by mixed noise with Gaussian blur at GB1, GB2, and GB3. Table 3 shows the numerical results of the restored images by
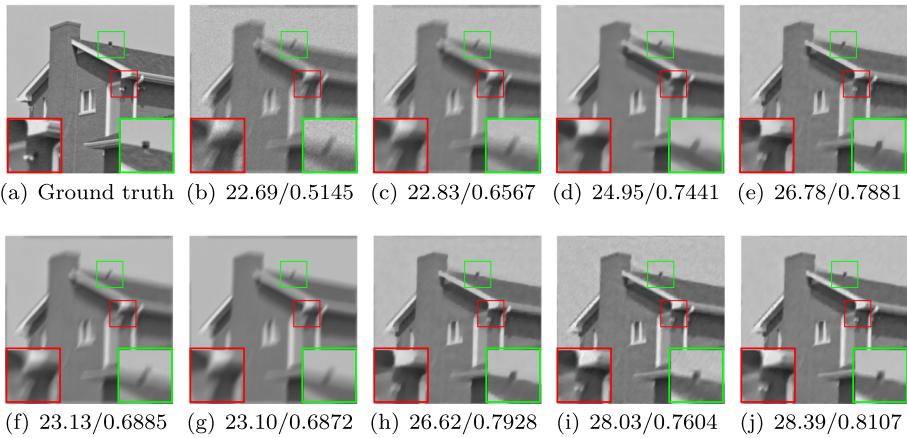
Fig. 5 The restoration results on "Test 1" with zoomed region and PSNR(dB)/SSIM values. **a** Ground truth. **b** Images degraded by MB(15, 60) with σ=1 and K=600. The denoising and deblurring results of: **c** DZ, **d** HNZ, **e** FL, **f** EM-CNN, **g** PARM, **h** TV model, **i** Mod. 1 and **j** ours, respectively
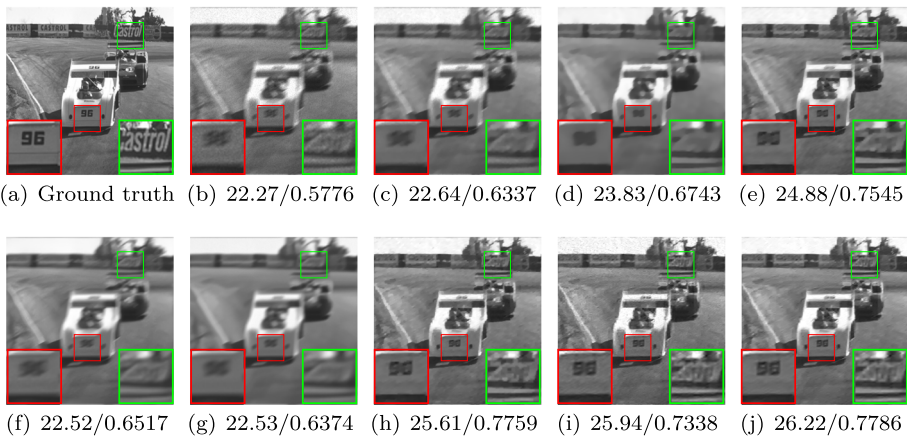

Fig. 6 The restoration results on "Test 5" with zoomed region and PSNR(dB)/SSIM values. **a** Ground truth. **b** Images degraded by MB(9, 30) with σ=1 and K=600. The denoising and deblurring results of: **c** DZ, **d** HNZ, **e** FL, **f** EM-CNN, **g** PARM, **h** TV model, **i** Mod. 1 and **j** ours, respectively

different methods and the better results are marked in black. Consequently, our method has the best numerical results at the average values of PSNR and SSIM.

Figures 7 and 8 show the image restoration results under mixed noise with Gaussian blur. As illustrated in Fig. 7, the recovery results of the DZ method, the HNZ method, the EM-CNN method, and the PARM method are too smooth and the texture details are blurred.

Specifically, the reconstructed images of the FL method and TV method have staircase effects, and we observe that the TV method and Mod. 1 are not completely denoised. However, our method yields the best visual effects in keeping the image sharp and removing noises. The situation in Fig. 8 is similar, we can see a significant step-up effect in the "shadows" of the red magnification areas in (e) and (f). Consequently, our method has the best image quality in terms of preserving edges and removing mixed noises.
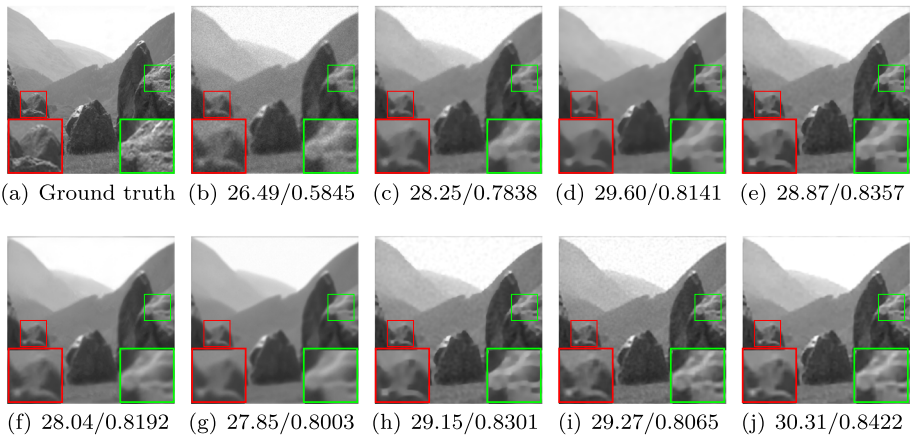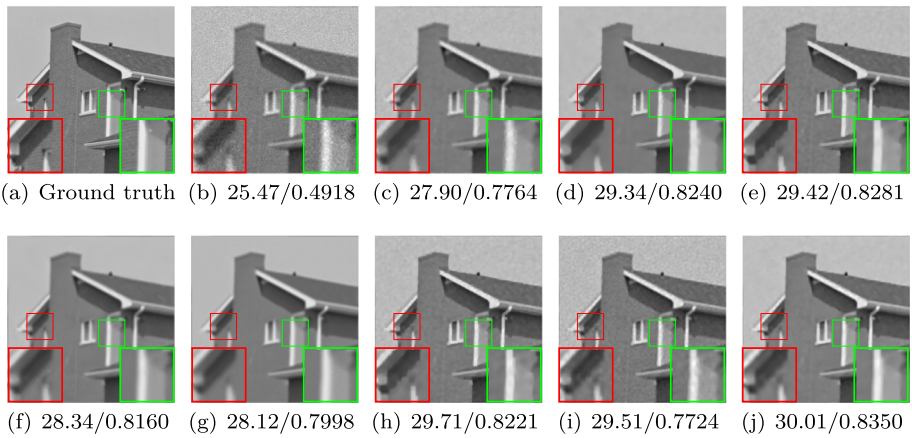
(a) Ground truth (b) 26.49/0.5845 (c) 28.25/0.7838 (d) 29.60/0.8141 (e) 28.87/0.8357

(f) 28.04/0.8192 (g) 27.85/0.8003 (h) 29.15/0.8301 (i) 29.27/0.8065 (j) 30.31/0.8422

Fig. 7 The restoration results on "Test 2" with zoomed region and PSNR(dB)/SSIM values. **a** Ground truth. **b** Images degraded by GB(5, 2) with σ=5 and K=600. The denoising and deblurring results of: **c** DZ, **d** HNZ, **e** FL, **f** EM-CNN, **g** PARM, **h** TV model, **i** Mod. 1 and **j** ours, respectively

(a) Ground truth (b) 25.47/0.4918 (c) 27.90/0.7764 (d) 29.34/0.8240 (e) 29.42/0.8281

(f) 28.34/0.8160 (g) 28.12/0.7998 (h) 29.71/0.8221 (i) 29.51/0.7724 (j) 30.01/0.8350

Fig. 8 The restoration results on "Test 1" with zoomed region and PSNR(dB)/SSIM values. **a** Ground truth. **b** Images degraded by GB(5, 2) with σ=5 and K=300. The denoising and deblurring results of: **c** DZ, **d** HNZ, **e** FL, **f** EM-CNN, **g** PARM, **h** TV model, **i** Mod. 1 and **j** ours, respectively

Figure 9 shows the denoised and deblurred results of residue on the "Test 1" image. In this sense, the noise residue of ours contains less useful information than the other models, and the solution contains more textures and structure [38].

4.5 Comparison of ADMM and sGS-imsPADMM Algorithm

In order to demonstrate the advantages of the sGS-imsPADMM algorithm, we compared the difference between the sGS-imsPADMM algorithm and the ADMM algorithm in terms of image restoration effect, CPU-time, and number of iterations. Numerical results are shown in Table 4. It can be seen that the ADMM algorithm requires more iterations and more time, and the sGS-imsPADMM is nearly 2 times faster than the ADMM algorithm. To visually demon-
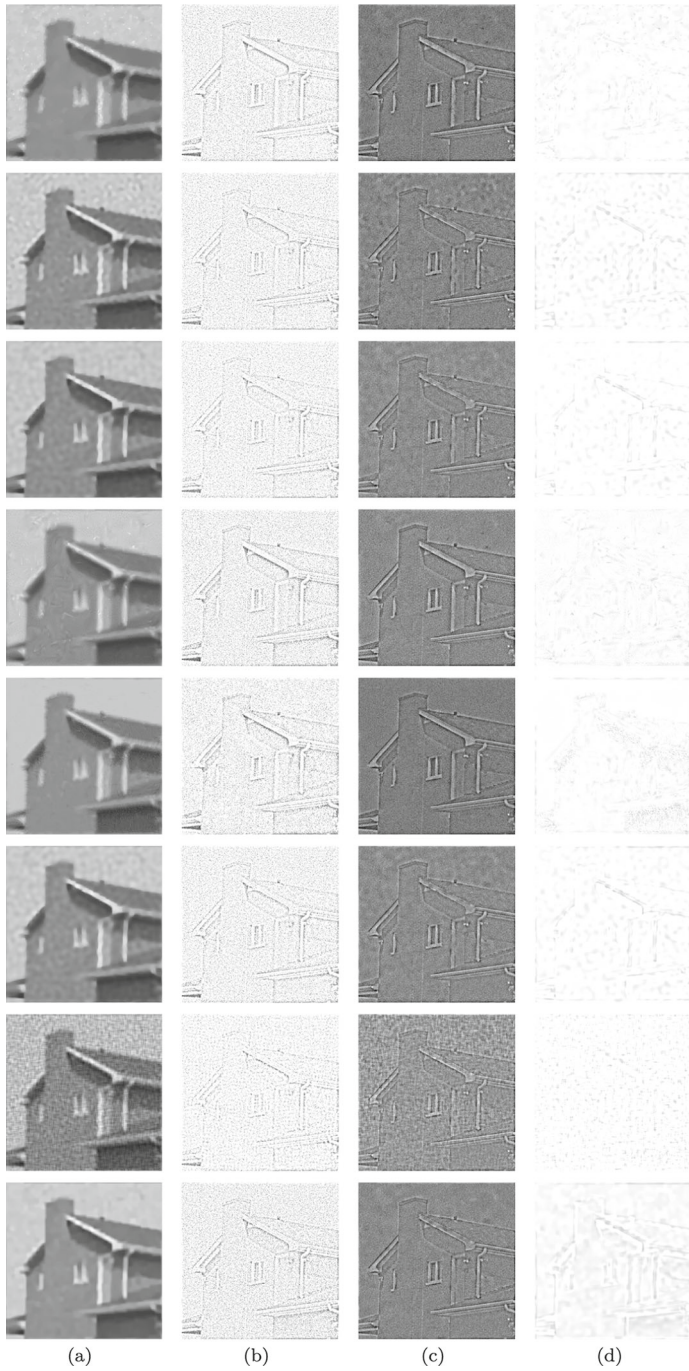
Fig. 9 The restoration results and the corresponding residual results. **a** The degraded images restored from "Test 1" at GB3 by different methods. **b** Gamma noise component. **c** Gaussian noise component. **d** Gaussian blur component. 1st row through 8th row: the restoration results of DZ, HNZ, FL, EM-CNN, PARM, TV model, Mod. 1 and ours, respectively
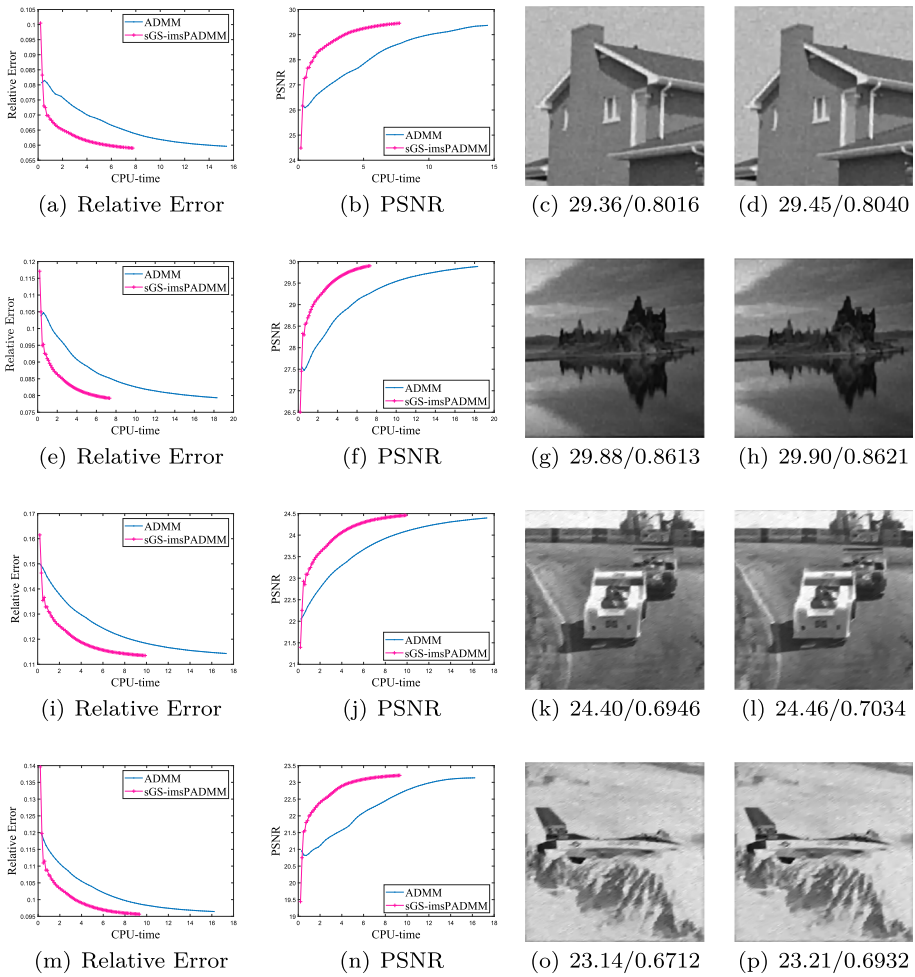
(a)　　　　　　(b)　　　　　　(c)　　　　　　(d)

Fig. 10 1st, 2nd column: The plots of relative error, PSNR with CPU-time. Blue line: ADMM. Red line: sGS-imsPADMM. 3rd, 4th column: The restoration results of ADMM, sGS-imsPADMM with PSNR(dB)/SSIM. **c–d**, **g–h** Images "Test 1, Test 3" are degraded by GB1. **k–l**, **o**–(**p**) Images "Test 5, Test 6" are degraded by MB1

strate the advantages of sGS-imsPADMM algorithm compared with the ADMM algorithm, we compared the plots of PSNR and relative error with CPU-time of sGS-imsPADMM algorithm and ADMM algorithm in Fig. 10. For convenience, we discussed the result of the image restoration on the "Test 1, Test 3" degraded by GB1 and the "Test 5, Test 6" degraded by MB1. Next, we compared the effects of two algorithms, ADMM and sGS-imsPADMM. Compared with the ADMM algorithm, the sGS-imsPADMM algorithm shows faster convergence effect.

5 Conclusion

In this paper, we presented a novel model for restoring blurred images with mixed noise, which incorporates wavelet tight frame regularization. The convexity of the model is ensured by a convexity-preserving term introduced in the model. Using sGS-imsPADMM with rela-

Table 4 The values of PSNR, SSIM, CPU-time in seconds and number of internal and external iteration steps

Deg	Image	Algorithm	PSNR (dB)	SSIM	CPU-time (s)	Inner	Outer
GB1	Test 1	ADMM	29.36	0.8016	14.60	245	77
		Ours	29.45	0.8040	7.74	127	63
	Test 2	ADMM	29.41	0.8054	18.85	324	103
		Ours	29.46	0.7911	10.31	171	85
	Test 3	ADMM	29.88	0.8613	18.31	279	89
		Ours	29.90	0.8621	7.34	111	59
MB1	Test 4	ADMM	28.87	0.6773	13.88	154	75
		Ours	29.07	0.6950	8.45	139	69
	Test 5	ADMM	24.40	0.6946	17.32	291	96
		Ours	24.46	0.7034	9.88	161	80
	Test 6	ADMM	23.14	0.6712	16.21	265	84
		Ours	23.21	0.6932	9.32	149	74

tive error control, we have effectively solved our proposed model and proved the convergence of the algorithm to a stationary point of the objective function. Our experiments have demonstrated that the proposed method outperforms several advanced methods and achieves the best image quality. Furthermore, the sGS-imsPADMM algorithm is nearly 2 times faster than ADMM. We have also successfully applied sGS-imsPADMM with relative error control for removing mixed noise and blur. In future work, we plan to explore the application of this algorithm to other problems, such as unknown types of noise with blur.

Data Availability Enquiries about data availability should be directed to the authors.

Declarations

Conflict of interest The authors declare that they have no Conflict of interest.

A: Appendix

A.1: Proof of Proposition 3

Proof For any given $z = (x, y, l) \in \mathcal{Z}$, we define $x_e := x - \bar{x}$, $y_e := y - \bar{y}$ and $l_e := l - \bar{l}$. Note that

$$\mathcal{R}\left(x_e^{k+1}, y_e^{k+1}\right) = \mathcal{R}\left(x^{k+1}, y^{k+1}\right) = (\vartheta\beta)^{-1}\left(l^{k+1} - l^k\right) = (\vartheta\beta)^{-1}\left(l_e^{k+1} - l_e^k\right). \tag{43}$$

Then, by using

$$d_y^{k+1} \in \partial_y L_\beta\left(x^{k+1}, y^{k+1}; z^k\right) + \mathcal{Q}\left(y^{k+1} - y^k\right), \tag{44}$$

we know that

$$d_y^{k+1} - \nabla g(y^k) - W^T \tilde{l}^{k+1} + \left(\Sigma_g + \mathcal{Q}\right) \Delta_y^k \in \partial q(y^{k+1}). \tag{45}$$

Now the KKT point $(\bar{x}, \bar{y}, \bar{l})$ (18) and the convexity of g implies that

$$\left\langle d_y^{k+1} + \nabla g(\bar{y}) - \nabla g(y^k) + W^T \bar{l} - W^T \tilde{l}^{k+1} + \left(\Sigma_g + \mathcal{Q}\right) \Delta_y^k, y_e^{k+1}\right\rangle \geq 0. \tag{46}$$

In addition, from Lemma 3, the above formula can be obtained

$$\left\langle d_y^{k+1} - W^T(\tilde{l}^{k+1} - \bar{l}) + \left(\Sigma_g + \mathcal{Q}\right) \Delta_y^k, y_e^{k+1}\right\rangle \geq \left\langle \nabla g(y^k) - \nabla g(\bar{y}), y_e^{k+1}\right\rangle \geq -\frac{1}{4}\left\|\Delta_y^k\right\|_{\Sigma_g}^2. \tag{47}$$

Similarly, for any $x \in \mathcal{X}$, combining (18) with (44), we have the following inequality

$$\left\langle -l^k - \beta\mathcal{R}(x^{k+1}, y^k) + \mathcal{P}\Delta_x^k, x_e^{k+1}\right\rangle \geq p(x^{k+1}) - p(\bar{x}) \geq -\left\langle \bar{l}, x_e^{k+1}\right\rangle. \tag{48}$$

Next, add up the above two inequalities to get (49)

$$\left\langle \left(\Sigma_g + \mathcal{Q}\right) \Delta_y^k + d_y^{k+1}, y_e^{k+1}\right\rangle + \left\langle \bar{l} - l^k - \beta\mathcal{R}(x^{k+1}, y^k), x_e^{k+1}\right\rangle$$
$$+ \left\langle W^T \bar{l} - W^T \tilde{l}^{k+1}, y_e^{k+1}\right\rangle + \left\langle \mathcal{P}\Delta_x^k, x_e^{k+1}\right\rangle \geq -\frac{1}{4}\left\|\Delta_y^k\right\|_{\Sigma_g}^2. \tag{49}$$

According to the Cauchy–Schwartz inequality, we obtain

$$\left\langle d_y^{k+1}, y_e^{k+1}\right\rangle \leq \frac{\nu}{2\epsilon_k^2}\left\|d_y^{k+1}\right\|_{\mathcal{N}^{-1}}^2 + \frac{\epsilon_k^2}{2\nu}\left\|y_e^{k+1}\right\|_{\mathcal{N}}^2$$
$$\leq \frac{\nu}{2}\left\|\Delta_y^k\right\|_{\mathcal{N}}^2 + \frac{\nu}{2}\left\|\Delta_y^{k-1}\right\|_{\mathcal{N}}^2 + \frac{\epsilon_k^2}{2\nu}\left\|y_e^{k+1}\right\|_{\mathcal{N}}^2. \tag{50}$$

Furthermore, we have the following two equations

$$\left\langle \left(\Sigma_g + \mathcal{Q}\right) \Delta_y^k + d_y^{k+1}, y_e^{k+1}\right\rangle$$
$$= \frac{1}{2}\left(\left\|y_e^k\right\|_{\Sigma_g+\mathcal{Q}}^2 - \left\|y_e^{k+1}\right\|_{\Sigma_g+\mathcal{Q}}^2\right) - \frac{1}{2}\left\|\Delta_y^k\right\|_{\Sigma_g+\mathcal{Q}}^2 + \left\langle d_y^{k+1}, y_e^{k+1}\right\rangle, \tag{51}$$

and

$$\left\langle \mathcal{P}\Delta_x^k, x_e^{k+1}\right\rangle = \frac{1}{2}\left(\left\|x_e^k\right\|_{\mathcal{P}}^2 - \left\|x_e^{k+1}\right\|_{\mathcal{P}}^2\right) - \frac{1}{2}\left\|\Delta_x^k\right\|_{\mathcal{P}}^2. \tag{52}$$

By using the definition of $\tilde{l}^{k+1}$, we have

$$
\begin{aligned}
\left\langle W^T \bar{l} - W^T \tilde{l}^{k+1}, y_e^{k+1} \right\rangle &+ \left\langle \bar{l} - l^k - \beta \mathcal{R}(x^{k+1}, y^k), x_e^{k+1} \right\rangle \\
&= \frac{1}{2} \left(\left\| y_e^k \right\|_{\beta I}^2 - \left\| y_e^{k+1} \right\|_{\beta I}^2 \right) + \frac{(\vartheta - 1)\beta}{2} \left\| r^{k+1} \right\|^2 \\
&+ \frac{1}{2\vartheta\beta} \left(\left\| l_e^k \right\|^2 - \left\| l_e^{k+1} \right\|^2 \right) - \frac{\beta}{2} \left\| \mathcal{R}(x^{k+1}, y^k) \right\|^2.
\end{aligned}
\tag{53}
$$

Substituting (50)–(53) into (49), we obtain (54)

$$
\begin{aligned}
\left\| \Delta_x^k \right\|_{\mathcal{P}}^2 &+ \left\| \Delta_y^k \right\|_{\frac{1}{2}\Sigma_g + \mathcal{Q}}^2 + (1 - \vartheta)\beta \left\| r^{k+1} \right\|^2 + \beta \left\| \mathcal{R}(x^{k+1}, y^k) \right\|^2 \\
&- \nu \left(\left\| \Delta_y^k \right\|_{\mathcal{N}}^2 - \left\| \Delta_y^{k-1} \right\|_{\mathcal{N}}^2 \right) \\
&\leq \frac{1}{\vartheta\beta} \left(\left\| l_e^k \right\|^2 - \left\| l_e^{k+1} \right\|^2 \right) + \left\| x_e^k \right\|_{\mathcal{P}}^2 - \left\| x_e^{k+1} \right\|_{\mathcal{P}}^2 \\
&+ \left\| y_e^k \right\|_{\mathcal{N}}^2 - (1 - \frac{\epsilon_k^2}{\nu}) \left\| y_e^{k+1} \right\|_{\mathcal{N}}^2.
\end{aligned}
\tag{54}
$$

Then, using Lemma 7 [22], we obtain the inequality

$$
\begin{aligned}
(1 - \vartheta)\beta \left\| r^{k+1} \right\|^2 &+ \beta \left\| \mathcal{R}(x^{k+1}, y^k) \right\|^2 \\
&\geq \left\| \Delta_y^k \right\|_{\Sigma_g + \mathcal{Q}}^2 - \left\| \Delta_y^{k-1} \right\|_{\Sigma_g + \mathcal{Q}}^2 + \omega \left(\left\| r^{k+1} \right\|^2 - \left\| r^k \right\|^2 \right) \\
&+ \beta \min\{\vartheta, 1 + \vartheta - \vartheta^2\} \left(\left\| \Delta_y^k \right\|_I^2 + \frac{1}{\vartheta} \left\| r^{k+1} \right\|^2 \right).
\end{aligned}
\tag{55}
$$

Substitute the inequality into (54) and using (32), we have

$$
\begin{aligned}
\phi_k(\bar{z}) &- \left(1 - \frac{\epsilon_k^2}{\nu} \right) \phi_{k+1}(\bar{z}) + \omega \left\| r^k \right\|^2 - (1 - \frac{\epsilon_k^2}{\nu})\omega \left\| r^{k+1} \right\|^2 - \frac{\epsilon_k^2}{\nu} \left\| x_e^{k+1} \right\|_{\mathcal{P}}^2 \\
&\geq \left\| \Delta_x^k \right\|_{\mathcal{P}}^2 + \left\| \Delta_y^k \right\|_{\frac{1}{2}\Sigma_g + \mathcal{Q}}^2 - 2\nu \left\| \Delta_y^k \right\|_{\mathcal{N}}^2 \\
&+ (1 - \vartheta + \min\{\vartheta, \vartheta^{-1}\}) \left(\vartheta \left\| \Delta_y^k \right\|_{\beta I}^2 + \beta \left\| r^{k+1} \right\|^2 \right) \\
&= \left\| \Delta_x^k \right\|_{\mathcal{P}}^2 + \left\| \Delta_y^k \right\|_{\mathcal{O}}^2 - 2\nu \left\| \Delta_y^k \right\|_{\mathcal{N}}^2 + \widehat{\omega} \left\| r^{k+1} \right\|^2.
\end{aligned}
\tag{56}
$$

So far, the inequality (33) holds, and the proof is complete. $\qquad\square$

A.2 Proof of Theorem 1

Proof Denote the self-adjoint linear operators:

$$
\begin{aligned}
\mathcal{J} &:= \mathrm{Diag}\left(\mathcal{P}, \mathcal{N}, \frac{1}{\vartheta\beta} I \right) + \left(\omega + \frac{1}{4}\widehat{\omega} \right) \mathcal{R}^T \mathcal{R}, \\
\mathcal{K} &:= \mathrm{Diag}\left(\mathcal{P}, \mathcal{O} - 2\nu\mathcal{N}, \frac{\widehat{\omega}}{4\beta^2\vartheta^2} I \right) + \frac{\widehat{\omega}}{8} \mathcal{R}^T \mathcal{R}.
\end{aligned}
\tag{57}
$$

According to Theorem 3.1 [9] and Proposition 4 [19], we have

$$
(1+v)\left\|\triangle_y^k\right\|_{\mathcal{G}}^2 + \left\|z^{k+1}-\bar{z}\right\|_{\mathcal{J}}^2
$$
$$
\leq \left(1+\frac{\epsilon_k^2}{4v}\right)\left(1+\frac{\epsilon_{k-1}^2}{4v}\right)\left((1+v)\left\|\triangle_y^{k-2}\right\|_{\mathcal{G}}^2 + \left\|z^{k-1}-\bar{z}\right\|_{\mathcal{J}}^2\right). \tag{58}
$$

Then, for integer j, we have

$$
(1+v)\left\|\triangle_y^k\right\|_{\mathcal{G}}^2 + \left\|z^{k+1}-\bar{z}\right\|_{\mathcal{J}}^2
$$
$$
\leq \prod_{i=j}^{k}\left(1+\frac{\epsilon_i^2}{4v}\right)\left((1+v)\left\|y^j-y^{j-1}\right\|_{\mathcal{G}}^2 + \left\|z^j-\bar{z}\right\|_{\mathcal{J}}^2\right) \tag{59}
$$
$$
\leq \prod_{k=0}^{\infty}\left(1+\frac{\epsilon_k^2}{4v}\right)\left((1+v)\left\|y^j-y^{j-1}\right\|_{\mathcal{G}}^2 + \left\|z^j-\bar{z}\right\|_{\mathcal{J}}^2\right).
$$

Therefore it can be concluded that there exists a constant $a' > 0$

$$
(1+v)\left\|\triangle_y^k\right\|_{\mathcal{G}}^2 + \left\|z^{k+1}-\bar{z}\right\|_{\mathcal{J}}^2 \leq a'.
$$

Then, we know that the sequence $\{z^k\}$ is bounded. Combine with Proposition 4 [19], we obtain

$$
\sum_{k=0}^{\infty}\left\|z^{k+1}-z^k\right\|_{\mathcal{K}}^2 \leq a' + a'\sum_{k=0}^{\infty}\frac{\epsilon_i^2}{4v} \leq +\infty. \tag{60}
$$

According to Lemma 2, we have $\sum_{k=1}^{\infty}\left\|e(z)^k\right\|^2 < +\infty$, $\lim_{k\to\infty}(z^{k+1}-z^k) = 0$, $\lim_{k\to\infty}\left\|z^{k+1}-z^k\right\|_{\mathcal{K}_1} = 0$ and $\lim_{k\to\infty}\left\|z^{k+1}-z^k\right\|_{\mathcal{K}_2} = 0$. Consequently, the subsequence $\{z^{k_i}\}$ converges to a cluster point z^∞. By using Lemma 2, letting $i \to \infty$, we have $e(z^\infty) = 0$. Because inequality (59) satisfies the KKT point condition, we have

$$
(1+v)\left\|\triangle_y^k\right\|_{\mathcal{G}}^2 + \left\|z^{k+1}-z^\infty\right\|_{\mathcal{J}}^2
$$
$$
\leq \prod_{k=0}^{\infty}\left(1+\frac{4\epsilon_k^2}{v}\right)\left((1+v)\left\|y^j-y^{j-1}\right\|_{\mathcal{G}}^2 + \left\|z^j-z^\infty\right\|_{\mathcal{J}}^2\right). \tag{61}
$$

Since for $i \to \infty$, $z^{k_i} \to z^\infty$, for any given $a > 0$, $i_0 > 0$, we obtain

$$
(1+v)\left\|y^{k_{i_0}}-y^{k_{i_0}-1}\right\|_{\mathcal{G}}^2 + \left\|z^{k_{i_0}}-z^\infty\right\|_{\mathcal{J}}^2 \leq \frac{a}{\prod_{k=0}^{\infty}\left(1+\frac{4\epsilon_k^2}{v}\right)}. \tag{62}
$$

Therefore, for any $k > k_{i_0}$, we have $\left\|z^k-z^\infty\right\|_{\mathcal{J}}^2 \leq a$. Note that $\mathcal{J} > 0$. Consequently, $\lim_{k\to\infty}z^k = z^\infty$, and the sequence $\{z_k\}$ converges to the KKT point. The proof is completed. $\square$

References

1. Ai, X., Ni, G., Zeng, T.: Nonconvex regularization for blurred images with Cauchy noise. Inverse Prob. Imaging **16**(3), 625–646 (2022)

2. Aubert, G., Aujol, J.F.: A variational approach to removing multiplicative noise. SIAM J. Appl. Math. **68**(4), 925–946 (2008)

3. Bao, C., Cai, J., Choi, J.K., Dong, B., Wei, K.: Improved harmonic incompatibility removal for susceptibility mapping via reduction of basis mismatch. J. Comput. Math. **40**(6), 913 (2022)

4. Baraha, S., Sahoo, A.K., Modalavalasa, S.: A systematic review on recent developments in nonlocal and variational methods for SAR image despeckling. Signal Process. **196**, 108521 (2022)

5. Cai, J.F., Choi, J.K., Li, J., Wei, K.: Image restoration: structured low rank matrix framework for piecewise smooth functions and beyond. Appl. Comput. Harmon. Anal. **56**, 26–60 (2022)

6. Cai, J.F., Osher, S., Shen, Z.: Linearized Bregman iterations for frame-based image deblurring. SIAM J. Imaging Sci. **2**(1), 226–252 (2009)

7. Cai, J.F., Shen, Z.: Framelet based deconvolution. J. Comput. Math. **28**(3), 289–308 (2010)

8. Chen, L., Sun, D., Toh, K.C.: An efficient inexact symmetric Gauss-Seidel based majorized ADMM for high-dimensional convex composite conic programming. Math. Program. **161**(1), 237–270 (2017)

9. Chen, L., Sun, D., Toh, K.C., Zhang, N.: A unified algorithmic framework of symmetric Gauss-Seidel decomposition based proximal ADMMs for convex composite programming. J. Comput. Math. **37**, 739–757 (2019)

10. Daubechies, I., Teschke, G., Vese, L.: Iteratively solving linear inverse problems under general convex constraints. Inverse Prob. Imaging **1**(1), 29 (2007)

11. Dong, Y., Zeng, T.: A convex variational model for restoring blurred images with multiplicative noise. SIAM J. Imaging Sci. **6**(3), 1598–1625 (2013)

12. Duan, Y., Zhong, Q., Tai, X.C., Glowinski, R.: A fast operator-splitting method for Beltrami color image denoising. J. Sci. Comput. **92**(3), 89 (2022)

13. Gu, S., Zhang, L., Zuo, W., Feng, X.: Weighted nuclear norm minimization with application to image denoising. In: Proceedings of the IEEE Conference on Computer Vision and Pattern Recognition (2014)

14. Huang, Y., Ng, M., Zeng, T.: The convex relaxation method on deconvolution model with multiplicative noise. Commun. Comput. Phys. **13**(4), 1066–1092 (2013)

15. Jon, K., Liu, J., Wang, X., Zhu, W., Xing, Y.: Weighted hyper-Laplacian prior with overlapping group sparsity for image restoration under Cauchy noise. J. Sci. Comput. **87**, 1–32 (2021)

16. Langer, A.: Locally adaptive total variation for removing mixed Gaussian-impulse noise. Int. J. Comput. Math. **96**(2), 298–316 (2019)

17. Lemaréchal, C., Sagastizábal, C.: Practical aspects of the Moreau-Yosida regularization: theoretical preliminaries. SIAM J. Optim. **7**(2), 367–385 (1997)

18. Li, C., Fan, Q.: A modified variational model for restoring blurred images with additive noise and multiplicative noise. Circuits Syst. Signal Process. **37**(6), 2511–2534 (2018)

19. Li, M., Wu, Z.: On the convergence rate of inexact majorized sGS ADMM with indefinite proximal terms for convex composite programming. Asia-Pacific J. Oper. Res. **38**(01), 2050035 (2021)

20. Li, X., Meng, X., Xiong, B.: A fractional variational image denoising model with two-component regularization terms. Appl. Math. Comput. **427**, 127178 (2022)

21. Li, X., Sun, D., Toh, K.C.: A block symmetric Gauss-Seidel decomposition theorem for convex composite quadratic programming and its applications. Math. Program. **175**, 395–418 (2019)

22. Lin, T., Ma, S., Zhang, S.: Iteration complexity analysis of multi-block ADMM for a family of convex minimization without strong convexity. J. Sci. Comput. **69**, 52–81 (2016)

23. Liu, J., Lou, Y., Ni, G., Zeng, T.: An image sharpening operator combined with framelet for image deblurring. Inverse Prob. **36**(4), 045015 (2020)

24. Liu, X., Lu, J., Shen, L., Xu, C., Xu, Y.: Multiplicative noise removal: nonlocal low-rank model and its proximal alternating reweighted minimization algorithm. SIAM J. Imaging Sci. **13**(3), 1595–1629 (2020)

25. Lu, J., Yang, Z., Shen, L., Lu, Z., Yang, H., Xu, C.: A framelet algorithm for de-blurring images corrupted by multiplicative noise. Appl. Math. Model. **62**, 51–61 (2018)

26. Lv, X.G., Li, F.: An iterative decoupled method with weighted nuclear norm minimization for image restoration. Int. J. Comput. Math. **97**(3), 602–623 (2020)

27. Lv, X.G., Li, F., Liu, J., Lu, S.T.: A patch-based low-rank minimization approach for speckle noise reduction in ultrasound images. Adv. Appl. Math. Mech. **14**(1), 155–180 (2022)

28. Lv, X.G., Song, Y.Z., Li, F.: An efficient nonconvex regularization for wavelet frame and total variation based image restoration. J. Comput. Appl. Math. **290**, 553–566 (2015)

29. Rockafellar, R.T.: Convex Analysis. Princeton University Press, Princeton (1997)

30. Rudin, L., Lions, P., Osher, S.: Multiplicative denoising and deblurring: theory and algorithms. Geom. Level Set Methods Imaging Vis. Graph. **4**, 103–120 (2003)

31. Rudin, L., Osher, S., Fatemi, E.: Nonlinear total variation based noise removal algorithms. Phys. D **60**, 259–268 (1992)

32. Shan, X., Sun, J., Guo, Z.: Multiplicative noise removal based on the smooth diffusion equation. J. Math. Imaging Vis. **61**, 763–779 (2019)
33. Shi, J., Osher, S.: A nonlinear inverse scale space method for a convex multiplicative noise model. SIAM J. Imag. Sci. **1**(3), 294–321 (2008)
34. Thanh, D., Dvoenko, S., Sang, D.: A mixed noise removal method based on total variation. Informatica **40**, 159–167 (2016)
35. Ullah, A., Chen, W., Khan, M.A., Sun, H.: An efficient variational method for restoring images with combined additive and multiplicative noise. Int. J. Appl. Comput. Math. **3**(3), 1999–2019 (2017)
36. Wang, F., Huang, H., Liu, J.: Variational-based mixed noise removal with CNN deep learning regularization. IEEE Trans. Image Process. **29**, 1246–1258 (2019)
37. Wang, Z., Bovik, A.C., Sheikh, H.R., Simoncelli, E.P.: Image quality assessment: from error visibility to structural similarity. IEEE Trans. Image Process. **13**(4), 600–612 (2004)
38. Yao, W., Guo, Z., Sun, J., Wu, B., Gao, H.: Multiplicative noise removal for texture images based on adaptive anisotropic fractional diffusion equations. SIAM J. Imaging Sci. **12**(2), 839–873 (2019)
39. Zhang, N., Wu, J., Zhang, L.: A linearly convergent majorized ADMM with indefinite proximal terms for convex composite programming and its applications. Math. Comput. **89**(324), 1867–1894 (2020)
40. Zhang, Y., Li, S., Guo, Z., Wu, B., Du, S.: Image multiplicative denoising using adaptive Euler's elastica as the regularization. J. Sci. Comput. **90**(2), 69 (2022)